Journal of Computational Physics **174,** 579–613 (2001)
doi:10.1006/jcph.2001.6897, available online at http://www.idealibrary.com on IDEAL®

Shallow Water Model on a Modified Icosahedral Geodesic Grid by Using Spring Dynamics

Hirofumi Tomita,* Motohiko Tsugawa,* Masaki Satoh,* and Koji Goto†

*Frontier Research System for Global Change, Integrated Modeling Research Program, 3173-25 Showamachi, Kanazawa-ku, Yokohama-city, Kanagawa, 236-0001, Japan; and †NEC, Scientific Software Department, Supercomputers Marketing Promotion Division 1-10, Nisshincho, Fuchu-city, Tokyo, 183-8501, Japan
E-mail: htomita@jamstec.go.jp

Received February 9, 2001; revised July 9, 2001

We develop a shallow water model on an icosahedral geodesic grid with several grid modifications. Discretizations of differential operators in the equations are based on the finite volume method, so that the global integrations of transported quantities are numerically conserved. Ordinarily, the standard grid is obtained by recursive grid division starting from the lowest order icosahedral grid. From the viewpoint of numerical accuracy of operators, we propose to relocate the variable-defined grid points from the standard positions to the gravitational centers of control volumes. From the other viewpoint of numerical stability, we modify the standard grid configuration by employing the spring dynamics, namely, the standard grid points are connected by appropriate springs, which move grid points until the dynamical system calms down. We find that the latter modification dramatically reduces the grid-noise in the numerical integration of equations. The reason for this is that the geometrical quantities of control volume such as its area and distortion of its shape exhibit the monotonic distribution on the sphere. By the combination of the two modifications, we can integrate the equations both with high accuracy and stability.

The performance of our model is examined by the standard test cases of shallow water model proposed by D. L. Williamson *et al.* (1992, *J. Comput. Phys.* **102**, 211). To investigate the convergence properties against resolution, we perform simulations from grid division level 4 (approximately $4.5^\circ \times 4.5^\circ$ grids) to 7 (approximately $0.56^\circ \times 0.56^\circ$ grids). The obtained results clearly indicate the advantage of use of our modified grid over the standard grid for the numerical accuracy and stability.

Key Words: shallow water model; modified icosahedral grid; spring dynamics; climate model.

0021-9991/01 $35.00

1. INTRODUCTION

The purpose of this paper is to propose a modified icosahedral grid configuration and to show excellent results from the time integration of the shallow water model using it. In this section, we attempt to provide some background to the present work by pointing out long-standing problems of grid models.

There are many applications in solving partial differential equation systems on a spherical geometry. One of them is in the geophysical fiuid dynamics, including the ocean and atmosphere dynamics. For numerically solving the ocean dynamics, the grid method has been used because of existence of land mass. On the other hand, most of today's atmospheric general circulation models employ the spectral method rather than the grid method to represent the meteorological fields. This is because the spectral method has the great advantage of high numerical accuracy over the grid method.

Recently, it was pointed out that the spectral method may not be suitable to high resolution simulations. One of the main reasons is the computational inefficiency of the Legendre transformation. In the representation of a field, the spherical harmonics are used as the basis functions, which consist of the associated Legendre functions and the trigonometric functions. When a nonlinear term is estimated, the transform between the wavenumber domain and the physical space is required. The Legendre transformation takes very high computational cost and the development of fast algorithm [1, 2] for it has not yet been completed. The operation time of total transformation increases as $O(n^3)$, where n is the total wavenumber. Another problem is related to the use of a massively parallel computer. The calculation of the nonlinear term by the spectral method essentially includes a process requiring all values on the global region. When the spectral method is employed on a distributed-memory architecture, it requires extensive data movement among computer nodes. Consequently, the ratio of communication to calculation becomes high and it makes the scalability of parallelization worse.

The grid method seems to be a good alternative to the spectral method. However, when the simple latitude–longitude grid is used, another problem, the so-called pole problem, occurs. The grid spacing near the poles becomes very small as the resolution becomes high. This causes a very severe limitation of the time interval for advection problem because of the CFL (Courant–Friedrich–Lewy) condition [3]. There are some techniques to overcome the pole problem. One of them is the filtering technique [4, 5]. High wavenumber components near the pole, which tend to appear as grid-scale noise, are removed explicitly. However, general consensus does not exist for what type of filter is the best and how filters should work. Furthermore, it is difficult in most cases to explain physical meaning of filters themselves. As another remedy for the pole problem, the semi-Lagrangian method [6] is applied to advection scheme. Using this method, we can be free from the CFL limitation. However, the simple semi-Lagrangian method does not guarantee the conservation of mass. To ensure it, some modifications may be required [7].

In order to radically overcome the pole problem, other types of grids, which are distributed as homogeneously as possible on the sphere, are needed One of such grids is the icosahedral grid. The idea of using icosahedral grids dates from 1960s. The original works in the meteorological area were performed by Sadourny *et al.* [8] and Williamson [9]. They solved the nondivergent barotropic equation by the finite difference method and examined the performance of the icosahedral grid for the Rossby–Haurwitz wave problem [10] with wavenumber 6. After those works, they extended the idea to primitive equations models

[11, 12]. Masuda and Ohnishi [13] also developed the primitive equations model, in which mass is exactly conserved. The conservations of kinetic energy and potential enstrophy are also considered in their model, though they are not complete. They also solved the Rossby–Haurwitz wave with several wavenumbers for their one-layer model (shallow water model). Another attempt was made to solve the problem not only by the finite difference method but also by the finite element method. Cullen [14] developed the shallow water model and Cullen and Hall [15] extended it to the multilayer model.

Although many efforts had been made, as described above, the icosahedral grid method as well as other grid methods were overwhelmed by the spectral method. This is because, besides the great advantage of numerical accuracy of spectral method, the development of fast Fourier transformation [16] somewhat reduced the high calculation cost of the transformation. However, as described previously, there still remains the problem caused by the Legendre transformation; that is, it becomes computationally more inefficient as the horizontal resolution increases.

Recently, several icosahedral grid systems including new ideas have been reconsidered in the planning of next-generation global models with very high horizontal resolution. Heikes and Randall [17, 18] developed a shallow water model on their modified icosahedral grid and tested the performance of their model by the standard test set proposed by Williamson *et al.* [19]. Their research group has extended it to a primitive equations model [20]. Stuhne and Peltier [21] developed a nondivergent barotropic model. They demonstrated that the use of icosahedral grid is free from the pole problem by applying their model to the barotropic instability problem near the pole. After that, they developed two shallow water models formulated by different forms of equations and compared the performances of these models [22]. Thuburn [23] independently developed a shallow water model, which has the conservation property for the potential vorticity.

Various grid construction methods using the icosahedron have been proposed. The method by Sadourny *et al.* [8] is that each of the triangle sides of spherical icosahedron is divided into n arcs and the grid points are connected along the geodesic line, where n is number of division. The method by Williamson [9] is somewhat different from that of Sadourny *et al*. [8]; after dividing the arcs of spherical icosahedron into n, perpendicular lines are drawn from the division points to the opposite sides and intersecting points are defined as grid points. The grid construction method used by Cullen [14] and Cullen and Hall [15] is similar to that of Sadourny *et al*. [8] but grid lines are not geodesic in their method. Another method is based on the recursive division technique. This method consists of the following procedures. Each side of the icosahedron whose vertices are on a unit sphere are projected onto the sphere. By connecting the midpoints of the geodesic arcs, four subtriangles are generated from each triangle. By iterating such a process, grid refinement proceeds. This simple method is employed by many recent researchs [17, 18, 20–23]. Heikes and Randall [17] modified the grid by twisting the icosahedral grid after first division to obtain the geometrical symmetry over the equator.

Although the icosahedral grid has the desirable property for the construction of high resolution geophysical models, that is, the spherical homogeneity of grid size, there still remain some problems to overcome. One of the problems in the use of icosahedral grid is the convergence problem of solution, that is, whether the numerical solution reasonably converges to the exact solution or not as the resolution increases. Actually, Stuhne and Peltier [22] reported the degradation of accuracy with increasing resolution in the standard test case 3 [19]. Heikes and Randall [17] also suggested that the result of the nonmodified

grid indicates a serious problem with regard to the accuracy of operators. They modified the grid to minimize the error of numerical operators [18].

In this paper, we describe the shallow water model on an icosahedral grid with new grid modifications. In particular, from the viewpoint of the accuracy of operators, we propose the relocation of grid points to the gravitational centers of control volumes. Furthermore, we propose the application of spring dynamics in the configuration of the modified icosahedral grid. This technique is expected to reduce the grid noise originated from the use of the Arakawa-A type grid. Combining these modifications, we perform numerical experiments to demonstrate high numerical accuracy and stability. In Section 2, the governing equations in this study are described. In Section 3, numerical implementation of the icosahedral grid to the governing equations is described. Differential operators in the governing equations are discretized by the finite volume method to conserve the global integration of mass. In Section 4, we describe our grid modification in detail and show the result of the operator test, which is similar to that used in Heikes and Randall [18]. In Section 5, the performance of our shallow water model using the modified grid is examined by the standard test set proposed by Williamson *et al*. [19] and also by several additional tests. We show the advantage of using the grid modified by our techniques. Finally, the concluding remarks and future directions are described in Section 6.

2. GOVERNING EQUATIONS

There are two forms in writing the momentum equation of the shallow water system: the vorticity-divergence form and the velocity form. In the vorticity-divergence form, the vorticity and divergence, which are invariant against the rotation of coordinate because of scalar quantities, are used as prognostic variables. If this formula is used, we have to solve the Poisson equation to obtain the velocity field from the vorticity and divergence. To numerically solve the Poisson equation, massive computational resources are required both in the calculation and in the communication. Stuhne and Peltier [21, 22] and Heikes and Randall [17] reduced the computational cost by using the multigrid technique. On the other hand, the velocity vector is directly solved in the velocity form. The velocity form would have some advantage over the vorticity-divergence form from the viewpoint of computational efficiency. For this reason, we employ the velocity form as the momentum equation. Stuhne and Peltier showed that the physical result of the velocity form is comparable with that of the vorticity-divergence form.

Côté [24] derived the three-dimensional form of the shallow water equations on the sphere as

$$\frac{\partial \mathbf{v}}{\partial t} + (\mathbf{v}\cdot\nabla)\mathbf{v} + f\hat{\mathbf{k}}\times\mathbf{v} = -\nabla(gh) - \frac{\mathbf{v}\cdot\mathbf{v}}{a}\hat{\mathbf{k}} \tag{1}$$

$$\frac{\partial h^*}{\partial t} + \nabla\cdot(h^*\mathbf{v}) = 0, \tag{2}$$

where $\mathbf{v}$ denotes the velocity vector that has three components but it lies on the tangential plane. h^* and h denote the fluid depth and the surface height, respectively. If h_s denotes the height of the underlying mountains, $h = h^* + h_s$. t is time, ∇ is gradient operator, and $\hat{\mathbf{k}}$ is vertical unit vector. f, g, and a are the Coriolis parameter, the gravitational acceleration, and the radius of the earth, respectively. The last term of Eq. (1) represents the constrained

force so as to satisfy the relation of $\hat{\mathbf{k}} \cdot \mathbf{v} = 0$. The second term on the left-hand side of Eq. (1) is rewritten as

$$(\mathbf{v} \cdot \nabla)\mathbf{v} = (\nabla \times \mathbf{v}) \times \mathbf{v} + \nabla\left(\frac{\mathbf{v} \cdot \mathbf{v}}{2}\right) \tag{3}$$

$$= \zeta \hat{\mathbf{k}} \times \mathbf{v} - \frac{\mathbf{v} \cdot \mathbf{v}}{a}\hat{\mathbf{k}} + \nabla\left(\frac{\mathbf{v} \cdot \mathbf{v}}{2}\right), \tag{4}$$

where ζ is vertical vorticity, defined as

$$\zeta = \hat{\mathbf{k}} \cdot (\nabla \times \mathbf{v}). \tag{5}$$

The detail derivation from Eq. (3) to Eq. (4) is described in Appendix A. From Eqs. (1) and (4), we can obtain the following vector invariant form:

$$\frac{\partial \mathbf{v}}{\partial t} + (\zeta + f)\hat{\mathbf{k}} \times \mathbf{v} = -\nabla\left(gh + \frac{\mathbf{v} \cdot \mathbf{v}}{2}\right). \tag{6}$$

We use Eq. (6) instead of Eq. (1) as the momentum equation. Thus, Eqs. (2) and (6) are the system equations to be solved in this study.

3. NUMERICAL METHOD

3.1. Spatial Discretization

The refinement of grid is done by the recursive technique, similar to that of Stuhne and Peltier [21, 22]. In this paper, the grid resolution obtained by l-th dividing operation is called "glevel l." Hereafter, the grid thus determined will be called the STD-grid. Figure 1 shows the STD-grid with glevel 3. The target resolutions in this study are from glevel 4 (approximately $4.5^\circ \times 4.5^\circ$ grids) to 7 (approximately $0.56^\circ \times 0.56^\circ$ grids).

We have an aim to extend our model to a climate model. In a long time-integration, such as climate simulation, conservations of quantities may be one of the most important

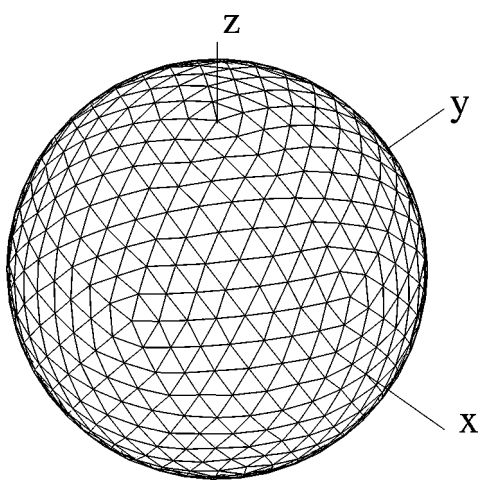

FIG. 1. The grid structure of the STD-grid with glevel 3.

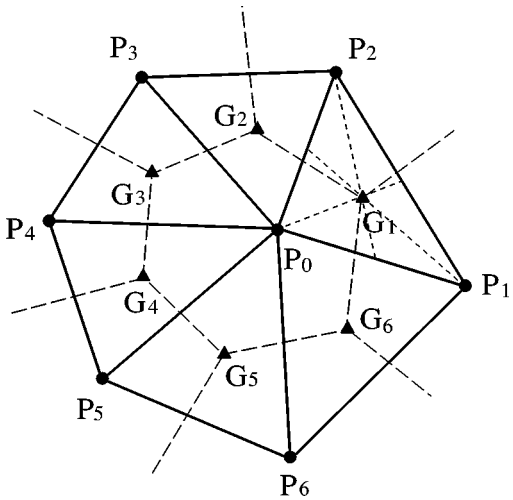

FIG. 2. Schematic figure of control volume in the STD-grid.

factors. For this reason, we employ the finite volume method for the discretization of differential operators. All variables are defined at the vertices of triangular grid elements. This arrangement is something like the Arakawa-A type grid. The schematic figure of control volume is shown in Fig. 2. The points denoted by black circles are the vertices of triangular grid elements, that is, variable-defined points. The points denoted by black triangles are the gravitational centers of triangular grid elements. The control volume for the point P_0 is the polygon constructed by connecting the gravitational centers of neighboring triangular grid elements. The shape of control volume is hexagon except that it is pentagon at only 12 points inherited from the original icosahedron.

In Eqs. (2) and (6), three differential operators appear: gradient operator (∇), divergence operator ($\nabla\cdot$), and curl operator ($\hat{\mathbf{k}}\cdot\nabla\times$). The divergence operator is discretized by the following method. If an arbitrary vector $\mathbf{u}$ at P_i in Fig. 2 is known, vector $\mathbf{u}$ at G_1 is calculated as

$$\mathbf{u}(G_1) = \frac{\alpha\mathbf{u}(P_0) + \beta\mathbf{u}(P_1) + \gamma\mathbf{u}(P_2)}{\alpha + \beta + \gamma}, \tag{7}$$

where α, β, and γ are the areas of $G_1P_1P_2$, $G_1P_2P_0$, and $G_1P_0P_1$, respectively. Vectors $\mathbf{u}$ at the other points $G_i (i = 2 \sim 6)$ are calculated in the same manner. If b_1 and $\mathbf{n}_1$ denote the geodesic arc length of G_1G_2 and the outward unit vector normal to this arc at the midpoint of G_1G_2, the outward flux f_1 crossing over the side G_1G_2 is estimated as

$$f_1 = b_1 \frac{\mathbf{u}(G_1) + \mathbf{u}(G_2)}{2} \cdot \mathbf{n}_1. \tag{8}$$

Other fluxes $f_i (i = 2 \sim 6)$ are also estimated in the same manner. From the Gauss theorem, we can obtain the divergence of $\mathbf{u}$ at the point P_0 as

$$\nabla \cdot \mathbf{u}(P_0) = \frac{1}{A(P_0)} \sum_{i=1}^{6} b_i \frac{\mathbf{u}(G_i) + \mathbf{u}\big(G_{1+\mathrm{mod}(i,6)}\big)}{2} \cdot \mathbf{n}_i, \tag{9}$$

where $A(P_0)$ is the area of control volume at the point P_0.

The curl operator and gradient operator are estimated in the similar manner of divergence operator; line integral values along the border of the control volume are divided by the area of control volume. If $\mathbf{m}_1$ denotes the counterclockwise unit vector parallel to the arc G_1G_2 at the midpoint, we can obtain the vertical component of $\nabla \times \mathbf{u}$ at the point P_0 as

$$\hat{\mathbf{k}} \cdot \nabla \times \mathbf{u}(P_0) = \frac{1}{A(P_0)} \sum_{i=1}^{6} b_i \frac{\mathbf{u}(G_i) + \mathbf{u}\left(G_{1+\mathrm{mod}(i,6)}\right)}{2} \cdot \mathbf{m}_i. \tag{10}$$

The gradient operator for an arbitrary variable q can be calculated as

$$\nabla_q(P_0) = \frac{1}{A(P_0)} \sum_{i=1}^{6} b_i \frac{q(G_i) + q\left(G_{1+\mathrm{mod}(i,6)}\right)}{2} \mathbf{n}_i - \frac{q_0}{A(P_0)} \sum_{i=1}^{6} b_i \mathbf{n}_i. \tag{11}$$

The second term of Eq. (11) is the correction term. If this term was neglected, the gradient vector of homogeneous field would not vanish because of the curvature of the spherical surface.

To continue numerically stable runs, we may add the fourth-order hyperviscosity term to the right-hand side of Eq. (6) as

$$\text{LHS of (6)} = \text{RHS of (6)} - \nu \nabla^4 \mathbf{v}, \tag{12}$$

where ν is the viscosity coefficient. We discretize this term as follows. Gradient vectors of velocity component at $G_i (i = 1 \sim 6)$ are calculated from values at three surrounding P_i points as in Eq. (11), but the correction term is omitted. The Laplacian at P_0 is obtained from divergence of the gradient vectors like Eq. (9). The discretization of the operator ∇^4 can be obtained by operating this process twice.

3.2. Temporal Scheme

All temporal integrations are performed explicitly. The third order Adams–Bashforth method is used as the temporal scheme as

$$\frac{\mathbf{V}^{n+1} - \mathbf{V}^n}{\Delta t} = \frac{1}{12} \left[23 \frac{\partial \mathbf{V}}{\partial t}\bigg|^{n} - 16 \frac{\partial \mathbf{V}}{\partial t}\bigg|^{n-1} + 5 \frac{\partial \mathbf{V}}{\partial t}\bigg|^{n-2} \right], \tag{13}$$

where $\mathbf{V} = (h, \mathbf{v})$. This scheme requires the temporal tendencies at two past time levels. Therefore, for two steps from the initial time, the fourth-order Runge–Kutta scheme is used. The time interval Δt is limited by the CFL condition of the gravity wave speed.

3.3. Other Computational Techniques

The data structure of variables in programming is similar to that of Stuhne and Peltier [21]; 10 rectangular regions are constructed by connecting two neighboring triangles of the original icosahedron. Such a structure of 10 rectangular regions is defined as region division level 0. We can divide regions by a scheme similar to that of grid division. Namely, four subrectangles are generated from each rectangle by connecting the diagonal mid-grid points. If this process is repeated n times, we can obtain the region structure of region division level n. All variables for each region can be described by a two-dimensional array

of Fortran. Data described above are designed in anticipation of the massively parallel computing based on vector processors.

In all calculations in this paper, the region division level is set to zero, so that the number of CPUs used is ten. The simulations are performed on a PC cluster,[1] in which the communication between computer nodes is performed by using Message Passing Interface (MPI).[2]

4. GRID MODIFICATION

Heikes and Randall [18] modified the grid structure to improve the accuracy of differential operators. In this section, in order to improve the accuracy of operators and to reduce the systematic grid noise, we propose a new modification method different from that of Heikes and Randall [18].

First, we consider the location of grid points as follows. Since operators at the grid point P_0 (Fig. 2) are discretized by the finite volume method as Eqs. (9)–(11), the values of the right-hand side in those equations represent average values in hexagonal or pentagonal control volumes. On the other hand, the values of the left-hand side represent the values at the grid point P_0. It is desirable that grid points should coincide with points whose values represent average values in the control volumes. It is natural to consider that the point representing the average value in the control volume should be the gravitational center of the control volume. However, it is not always so in the original STD-grid. Therefore, we move the location of the grid point to the gravitational center of the control volume. A schematic diagram of this process is shown in Fig. 3. We call the modified grid system the STD-GC-grid. This modified grid system provides the increase of accuracy for numerical operators. The mathematical proof for this property is given in Appendix B. Furthermore, it provides consistency with the governing equations in that the other volume forces, such as Coriolis force appearing in Eq. (6), are defined at the gravitational center of control volume.

As proposed by Heikes and Randall [18], we introduce the test functions,

$$\alpha(\lambda, \theta) = \sin(\lambda), \tag{14}$$

$$\beta(\lambda, \theta) = \cos(m\lambda)\cos^4(n\theta), \tag{15}$$

where λ and θ are longitude and latitude and m and n are arbitrary integers. Using these functions, we define a vector $\mathbf{u}$ as

$$\begin{aligned}\mathbf{u} &= \alpha\nabla\beta \\ &= \mathbf{i}\left[-m\frac{\cos^4(n\theta)}{\cos(\theta)}\sin(\lambda)\sin(m\lambda)\right] + \mathbf{j}[-4n\cos^3(n\theta)\sin(n\theta)\sin(\lambda)\cos(m\lambda)],\end{aligned} \tag{16}$$

where $\mathbf{i}$ and $\mathbf{j}$ are longitudinal and latitudinal unit vectors, respectively. We numerically calculate $\nabla\cdot\mathbf{u}$, $\hat{\mathbf{k}}\cdot(\nabla\times\mathbf{u})$, and $\nabla\beta$ by using Eqs. (9)–(11), respectively. These are compared with the exact solutions. Numerical errors are estimated by using one norm, two norm, and

[1] See http://www.beowulf.org/.

[2] See http://www.mpi-forum.org/.

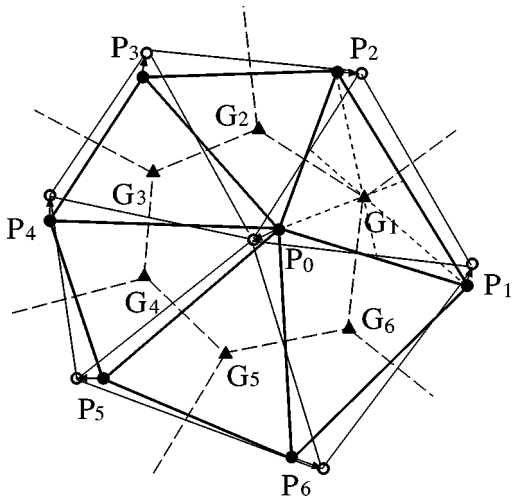

FIG. 3. Schematic figure of control volume in the STD-GC-grid.

infinity norm defined a

$$l_1(x) = \frac{I[|x(\lambda,\,\theta) - x_t(\lambda,\,\theta)|]}{I[|x_t(\lambda,\,\theta)|]}$$

$$l_2(x) = \frac{\{I[(x(\lambda,\,\theta) - x_t(\lambda,\,\theta))^2]\}^{1/2}}{\{I[x_t(\lambda,\,\theta)^2]\}^{1/2}}$$

$$l_\infty(x) = \frac{\max_{all\,\lambda,\,\theta} |x(\lambda,\,\theta) - x_t(\lambda,\,\theta)|}{\max_{all\,\lambda,\theta} |x_t(\lambda,\,\theta)|}, \tag{17}$$

where x represents either a scalar or a vector and I denotes the global-averaged operator; x_t denotes the exact value of x; l_1 and l_2 norms represent globally averaged errors; and l_∞ norm represents the maximum error in the global region.

Table I shows the norms for $m = 1$ and $n = 1$ with glevel 5. For all norms and all operators, the results of the STD-GC-grid are improved in comparison with those of STD-grid. Especially, the l_∞ norms are much improved. This means that the local errors are much reduced by the gravitational-centered modification.

To examine the error distribution on the sphere, we perform the following test. Solid rotation field (**v**) whose rotation axis corresponds to z-axis as shown in Fig. 1 is set to the grid points and its divergence ($\nabla \cdot \mathbf{v}$) is numerically solved. Since $\nabla \cdot \mathbf{v} = 0$ analytically, a numerical value of $|\nabla \cdot \mathbf{v}|$ indicates the difference from the exact solution. Figure 4a shows the distribution of $|\nabla \cdot \mathbf{v}|$ for the STD-GC-grid with glevel 5. Relatively large errors appear along the edge of triangles generated by the grid construction described in the previous section. In this case, the primary errors are on the lines of glevel 1 boundaries. The secondary errors are on the lines of glevel 2.

We define two geometrical quantities of control volume. One is its area denoted by A and the other is the distortion of its shape, which is defined as

$$S = \left[\left\{ \sum_{i=1}^{6} (l_i - l_{\text{mean}})^2 \right\} \Big/ 6 \right]^{1/2} \Big/ l_{\text{mean}}, \tag{18}$$

TABLE I
Comparison of Accuracies of the Differential Operators among the STD-Grid and the STD-GC Grid

Divergence operator			
	l_1	l_2	l_∞
STD-grid	3.580×10^{-3}	3.579×10^{-3}	7.194×10^{-3}
STD-GC-grid	2.981×10^{-3}	2.753×10^{-3}	2.546×10^{-3}
Rotation operator			
	l_1	l_2	l_∞
STD-grid	2.721×10^{-3}	2.936×10^{-3}	6.273×10^{-3}
STD-GC-grid	2.169×10^{-3}	2.086×10^{-3}	5.568×10^{-3}
Gradient operator			
	l_1	l_2	l_∞
STD-grid	2.295×10^{-3}	2.764×10^{-3}	8.882×10^{-3}
STD-GC-grid	1.830×10^{-3}	1.861×10^{-3}	2.814×10^{-3}

where l_i denotes the side length of control volume and l_{mean} is the reference length estimated from the area of control volume, which is defined as

$$l_{\text{mean}} = \left(\frac{2}{3\sqrt{3}} A \right)^{1/2}. \tag{19}$$

Figures 4b and 4c show the distributions of A and S. As shown in Fig. 4b and 4c, the recursive method of grid construction leads to a fractal structure in regard to the geometrical quantities of control volume; the differences from the mean values originate from the first division of grid construction. These differences are inherited to the next refined grid system at the second division. Thus, the grid system inherits the geometrical quantities from its previous generation. Comparing with Fig. 4a, it is seen that the region where a large error of numerical solution exists strongly corresponds to the region where the gradients of area and distortion of control volume are steep. The error pattern of $|\nabla \times \mathbf{v}|$ is similar to those of area and distortion, so that it may cause the generation of systematic grid noise at the temporal evolution of governing equations.

We can easily guess from the above discussion that if we construct a grid system in which geometrical quantities vary monotonically on the sphere, the error distribution on this grid system would be also monotonic so that the grid noise is reduced. To construct such a grid system, we propose an application of spring dynamics as follows. After the grid is constructed by the recursive method, grid points are connected by appropriate springs. Figure 5 shows the schematic figure of this process. The mathematical expression of this dynamic system can be described as

$$\sum_{i=1}^{6} k(d_i - \bar{d})\mathbf{e}_i - \alpha \mathbf{w}_0 = M \frac{d\mathbf{w}_0}{dt} \tag{20}$$

$$\mathbf{w}_0 = \frac{d\mathbf{r}_0}{dt}, \tag{21}$$

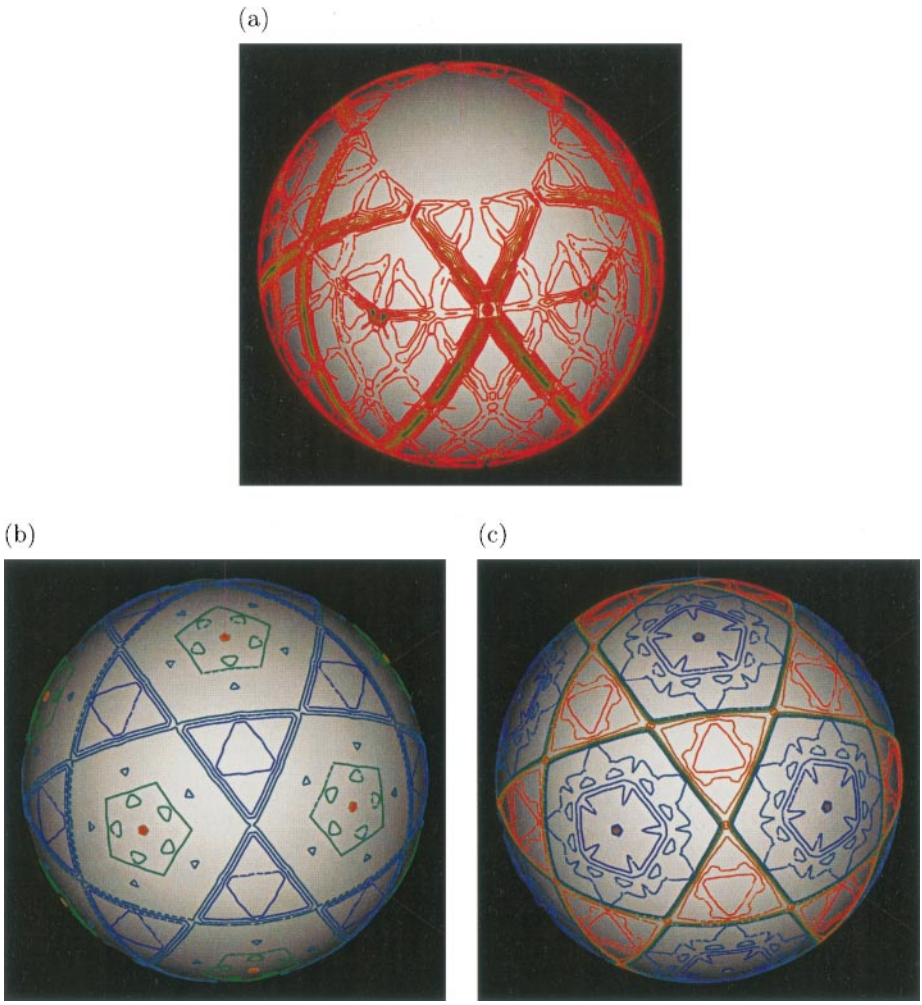

FIG. 4. (a) Error distribution of the divergence operator, (b) distribution of area of control volume, and (c) distribution of distortion of control volume for the STD-GC-grid. The values increase as color order of red, green, and blue.

where k is spring constant, d_i and $\bar{d}$ are the length of arc P_0P_i, and the length of spring without imposed force, respectively, $\mathbf{e}_i$ is unit vector in the direction from P_0 to P_i on the tangential plain at P_0, α is the frictional constant, $\mathbf{w}_0$ is the velocity vector at P_0, M is an arbitrarily defined mass, and $\mathbf{r}_0$ is the position vector of P_0. When the system calms down to the static balance, $\mathbf{w}_0 = 0$ and $d\mathbf{w}_0/dt = 0$, so that the following relation is satisfied:

$$\sum_{i=1}^{6}(d_i - \bar{d})\mathbf{e}_i = 0. \tag{22}$$

Thus, the grid can be obtained only by tuning $\bar{d}$, which is formulated using the grid division level l as

$$\bar{d} = \beta\frac{2\pi a}{10 \times 2^{l-1}}, \tag{23}$$

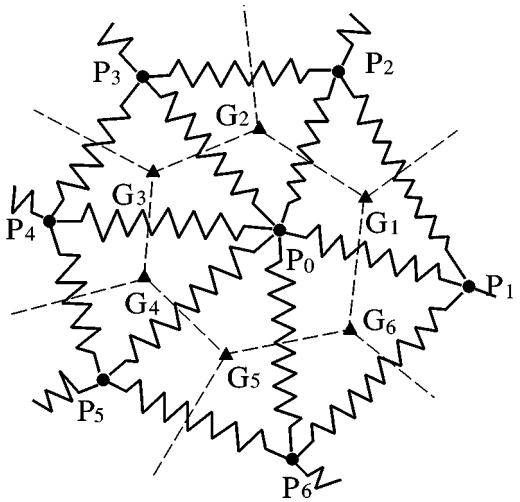

FIG. 5. Schematic figure of connection of spring in the modification using spring dynamics.

where β is the tuning parameter. The numerator and denominator on right-hand side of Eq. (23) represent the length of the equator and the number of grid points on the equator. In this study, we set $\beta = 0.4$. By using the STD-grid as the initial condition, Eqs. (20) and (21) are numerically solved until the balance equation (22) is satisfied. After that, control volumes are defined and grid points are moved to the gravitational centers of the control volumes in the same way as STD-GC-grid (Fig. 3). We call this grid the SPR-GC-grid. Figure 6 shows the SPR-GC-grid with glevel 3. Comparing the SPR-GC-grid (Fig. 6) with the STD-grid (Fig. 1), grid lines of the SPR-GC-grid are more smoothly curved than those of STD-grid, especially, near the 12 singular points. Instead, the grid intervals of the SPR-GC-grid near the singular points are a little smaller than those of STD-grid. In Appendix C, we discuss this problem and propose a countermeasure to it.

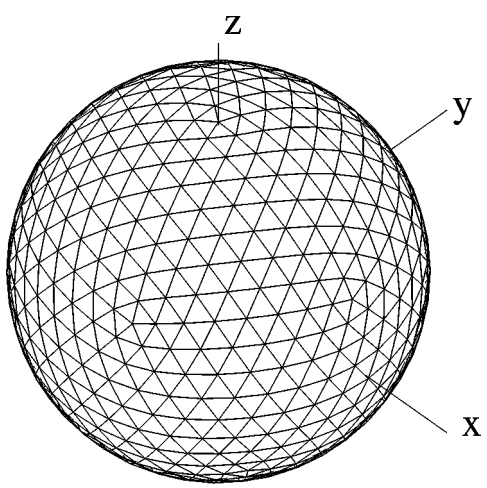

FIG. 6. The grid structure of the SPR-GC-grid with glevel 3.

Figure 7 shows the geometrical quantities and the error of divergence. The distributions of area and distortion of control volume show monotonic variations on the sphere. Consequently, the error distribution has also monotonicity and the noise-like error as shown in Fig. 4a disappears.

In order to check the convergence property of the SPR-GC-grid as increasing the resolution, we perform the operator test of $\nabla\beta$, $\nabla \cdot \mathbf{u}$, and $\hat{\mathbf{k}} \cdot (\nabla \times \mathbf{u})$ using Eqs. (14)–(16) for higher modes of $m = 3$ and $n = 3$. The convergences of l_2 and l_∞ norms defined by Eq. (17) for each of operators are shown in Fig. 8. For the STD-grid, the l_2 norms are reduced by a factor of four with each increment of glevel. In this sense, l_2 norms for the STD-grid vanish with the second order. However, the convergence speeds for the l_∞ norms become slower for higher resolution. For example, for the STD-grid, $l_\infty(\hat{\mathbf{k}} \cdot (\nabla \times \mathbf{u}))$ becomes only half with the increment of glevel as shown in Fig. 8c. On the other hand, for the SPR-GC-grid, both l_2 and l_∞ norms are reduced by a factor of four for all the operators.

5. NUMERICAL RESULTS

The suite of test cases proposed by Williamson *et al.* [19] has been used to investigate the performance of our shallow water model. There are seven cases in the suite. Our results of test case 1 and 4 are similar to those of Heikes and Randall's model [17]. We describe the results of test case 2, 3, 5, 6, and 7 in the following.

5.1. Test Case 2: Global Steady State Nonlinear Zonal Geostrophic Flow

This test case has a steady state solution of the nonlinear shallow water equations. The initial condition of the velocity field represents a solid body rotation, and the height field is in the geostrophic balance. The rotation axis of solid rotation can be chosen in any direction in the spherical coordinate and the Coriolis parameter becomes a function of longitude and latitude as

$$f = 2\Omega(-\cos\lambda\cos\theta\sin\alpha + \sin\theta\cos\alpha), \tag{24}$$

where α is angle between the rotation axis and the coordinate axis. Williamson *et al.* [19] suggest that tests should run with $\alpha = 0.0,\ 0.05,\ \pi/2$, and $\pi/2 - 0.05$. We set the same parameters u_0 and gh_0 as described in Eqs. (90)–(96) in Williamson *et al.* [19]. The numbers of time steps are set as 593, 1185, 2370, and 4740 in simulations for glevel 4, 5, 6, and 7, respectively. The corresponding time intervals are similarly equal to 728, 364, 182, and 91 s. All the cases are run without hyperviscosity.

Figure 9a shows the temporal histories of $l_\infty(h)$ norm for $\alpha = 0$ using the STD-grid, the STD-GC-grid, and the SPR-GC-grid. The $l_\infty(h)$ norm of the STD-grid is larger than the others even in the first stage and it becomes much larger as time goes on. This is because the operators in the case of the STD-grid are less accurate than those in the other grids. The $l_\infty(h)$ norm of the STD-GC-grid has a similar history to that of the SPR-GC-grid until $t = 1$ day, but it becomes large after $t = 1$ day. The reason why the result of the STD-GC-grid becomes worse is that, although the discretized operators of the STD-GC-grid are more accurate than those of the STD-grid, the discretized operators include

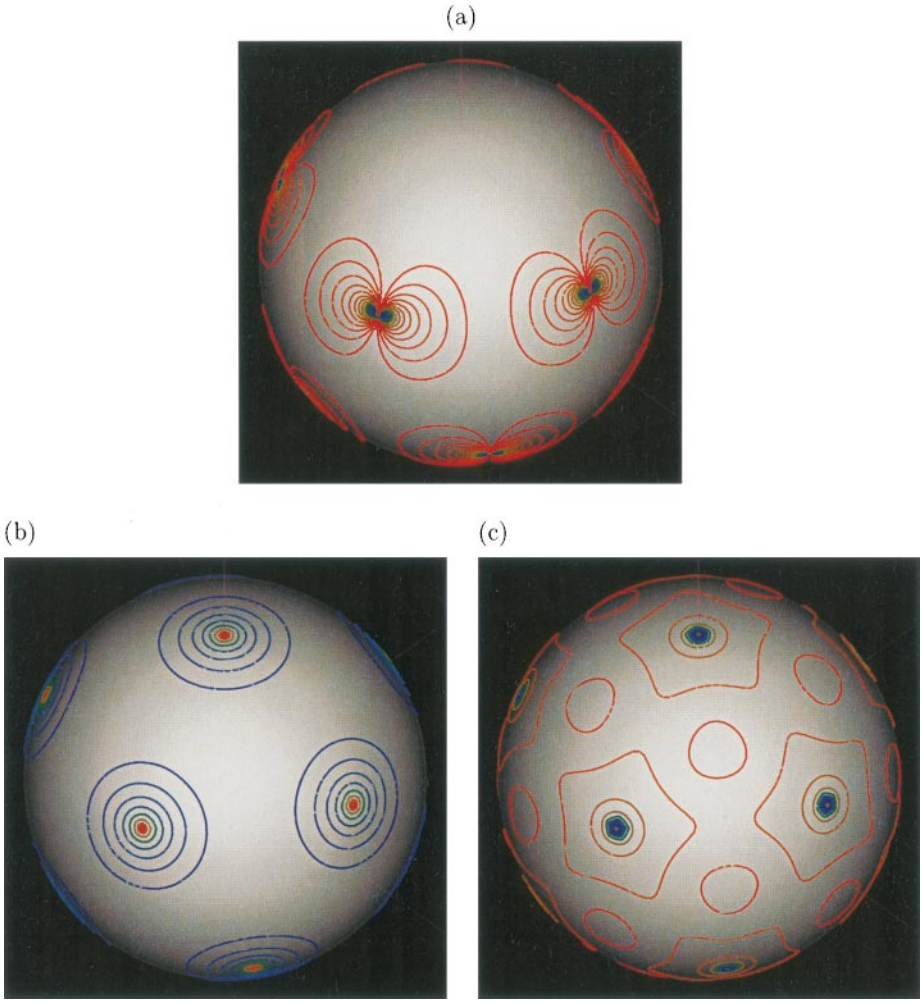

FIG. 7. (a) Error distribution of the divergence operator, (b) distribution of area of control volume, and (c) distribution of distortion of control volume for the SPR-GC-grid. The contour intervals are same as those in Fig. 4.

the systematic errors as shown in Fig. 4a so that a small grid noise, which occurs initially, is amplified and finally the whole field is contaminated by the noise. Although there is a small noise also in the case of the SPR-GC-grid, it is not amplified. Consequently, the $l_\infty(h)$ norm of the SPR-GC-grid is kept at almost the same values of the initial 1 day during 5 days.

Four runs of different α for glevel 5 are performed using the SPR-GC-grid. The rotation axis intersects the vertices of the major spherical triangles for the case of $\alpha = 0$, while the rotation axis penetrates the center of major spherical triangles for the case of $\alpha = \pi/2$. The results shown in Fig. 9b indicate little difference among the four cases. We may say that this is due to the isotropy of grid structure.

Figure 10 shows the dependence on the resolution using the SPR-GC-grid. The $l_2(h)$ norm is reduced by a factor of four with each increase in grid division level. The $l_\infty(h)$ norm also is reduced by a factor of four. The results for the velocity field **v** also indicates

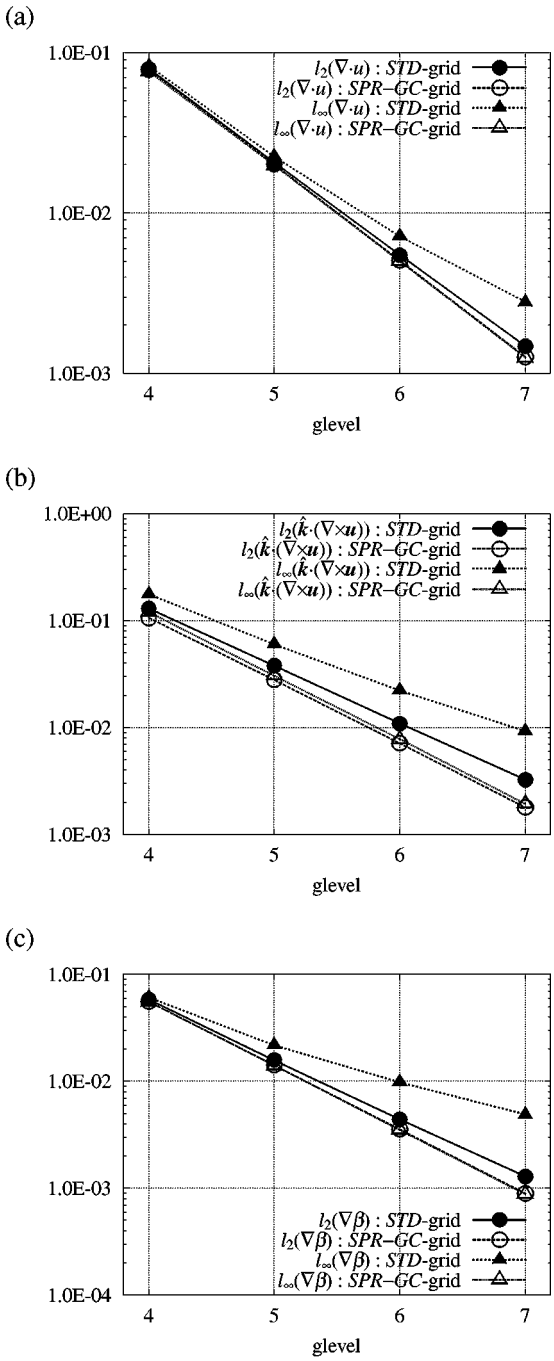

FIG. 8. Convergence properties of error norms for $m = 3$ and $n = 3$. (a) Divergence operator, (b) rotation operator, and (c) gradient operator.

similar convergence. Thus, for the prognostic variables, the second-order accuracy can be kept in both the global and the local sense.

The results of $l_\infty(h)$ for glevel 5 and $\alpha = 0$ are shown in the Fig. 8 of Heikes and Randall [17] and Fig. 2 of Stuhne and Peltier [22]. The $l_\infty(h)$ norm of the former maintains a value of

$1 \sim 2 \times 10^{-4}$ with some fluctuations. That of the latter is about 5×10^{-4}, which is the best value in their runs (vsw5). As shown in Fig. 10b, our $l_\infty(h)$ has a value around 2×10^{-4}, so that our value is comparable to that of Heikes and Randall [17] and is somewhat better than that of Stuhne and Peltier [22].

In the discretized system equations, there are two factors which generate higher wavenumber components. One is the nonlinear effect and the other is associated with discretized schemes. If the nonlinear effect is dominant, the viscosity term should be added to dissipate the high wavenumber components. This test case is free from the nonlinear effect, because the exact solution is steady. In this sense, we can regard this test case as the test to measure how long the model runs without viscosity. As previously shown in Fig. 9a, the result using the SPR-GC-grid indicates good accuracy and high stability. Although the originally proposed integration time of test case 2 is 5 days, we extend the integration time to 3 months. Figure 11 shows the temporal histories of $l_\infty(h)$ norm for the SPR-GC-grid with glevel 6 and 7. The level of values of $l_\infty(h)$ remains unchanged from the beginning to 90 days. We may say that the use of the SPR-GC-grid is the best choice in grid structures from the viewpoint of numerical stability.

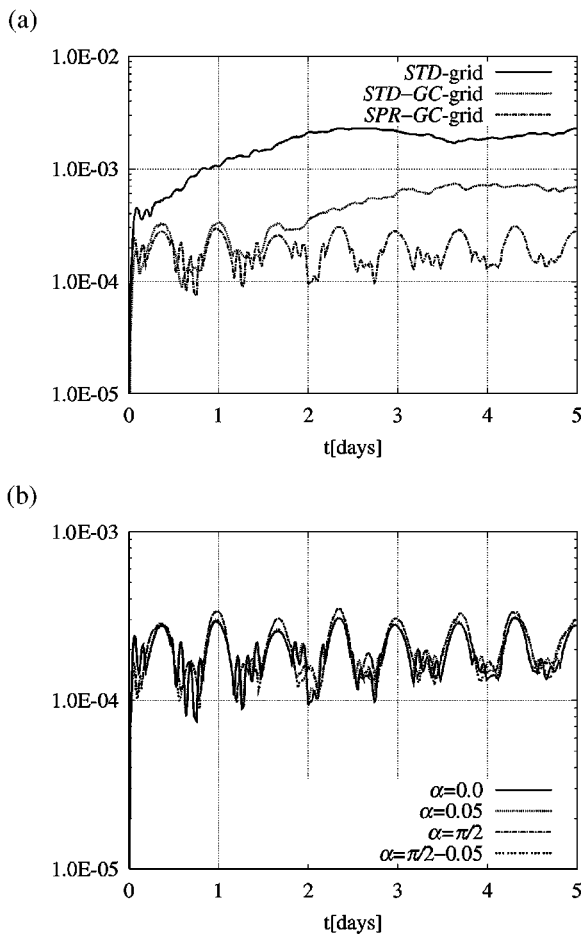

FIG. 9. The temporal variation of $l_\infty(h)$ norm for test case 2 (glevel 5). (a) Comparison between the grid systems for $\alpha = 0$ and (b) comparison between different values of α for the SPR-GC-grid.

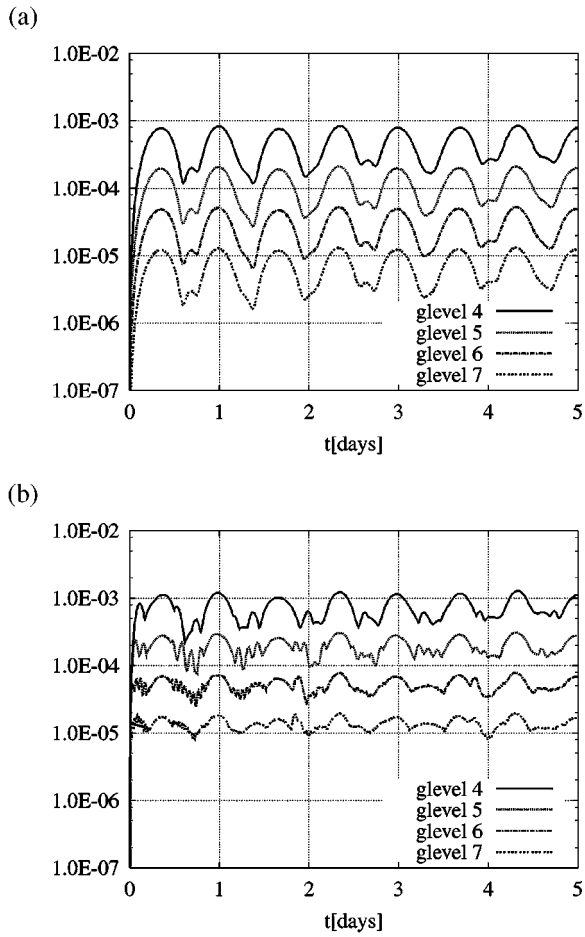

FIG. 10. The dependence of error norms on the resolution for test case 2 with $\alpha = 0$ (SPR-GC-grid). (a) The $l_2(h)$ norm and (b) the $l_\infty(h)$ norm.

5.2. Test Case 3: Steady State Nonlinear Zonal Geostrophic Flow with Compact Support

This test case was designed by Browning *et al.* [25]. The velocity field is a zonal flow as in test case 2, but the nonzero velocity region is confined in a range of latitude, that is,

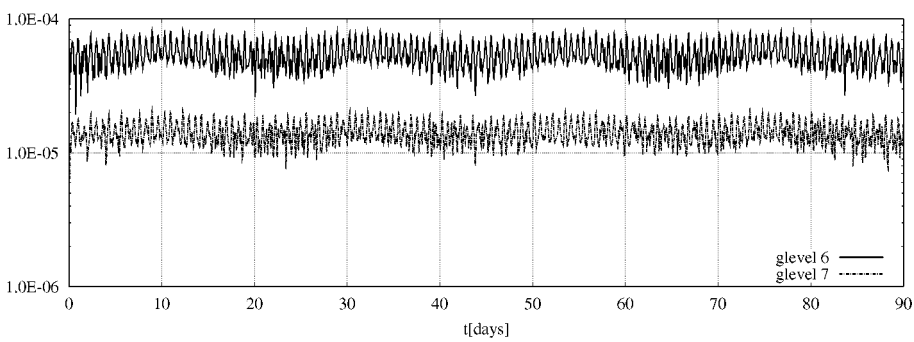

FIG. 11. The temporal variation of $l_\infty(h)$ norm for the 90 days integration of test case 2 with $\alpha = 0$.

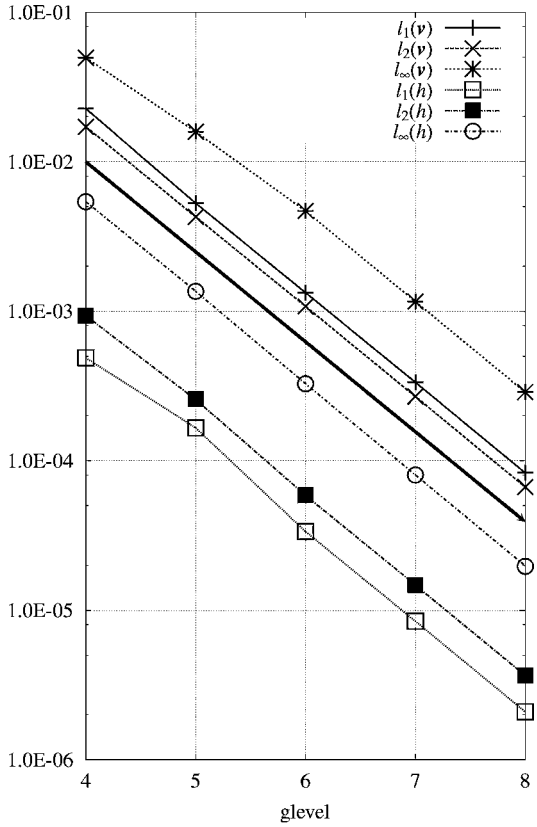

FIG. 12. Convergence properties of error norms by the grid refinement test for test case 3 with $\alpha = \pi/3$. Solid thick line represents the ideal quadratic convergence.

the jet flows in the midlatitude. The height field is in the geostrophic balance. The exact solution is steady. The initial conditions used are given in Eqs. (101)–(115) of Williamson *et al.* [19]. The angle between rotation axis and coordinate axis is set as $\alpha = 0$ and $\alpha = \pi/3$.

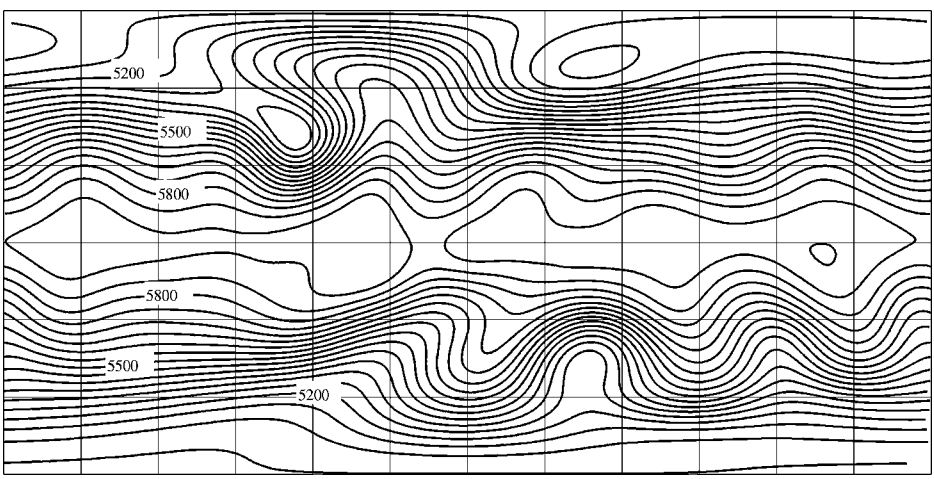

FIG. 13. Height field at the 15 days for the SPR-GC-grid with glevel 6.

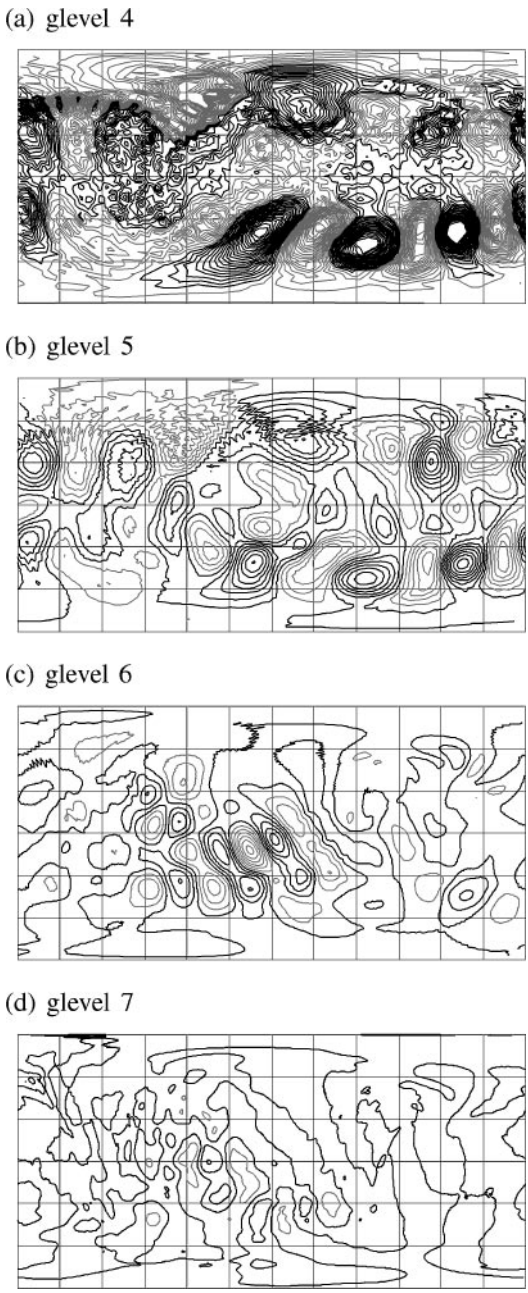

FIG. 14. Height field differences from the spectral result of T-213 for test case 5. Contour interval is 5 m. Solid lines and shaded lines indicate the positive and negative, respectively.

Williamson *et al.* [19] proposed a mesh convergence test for $\alpha = \pi/3$. Stuhne and Peltier [22] reported the degradation of accuracy with an increase in grid division level in this test case. Figure 3 of their paper [22] shows the increase of values for several error norms if the grid is refined from glevel 5 to 7. Heikes and Randall [17] reported that the twig10242 (glevel 5) results are quite a bit better than those of twig02562 (glevel 4). Their Fig. 9 shows that the norms of twig10242 are only half of those of twig02562, indicating the

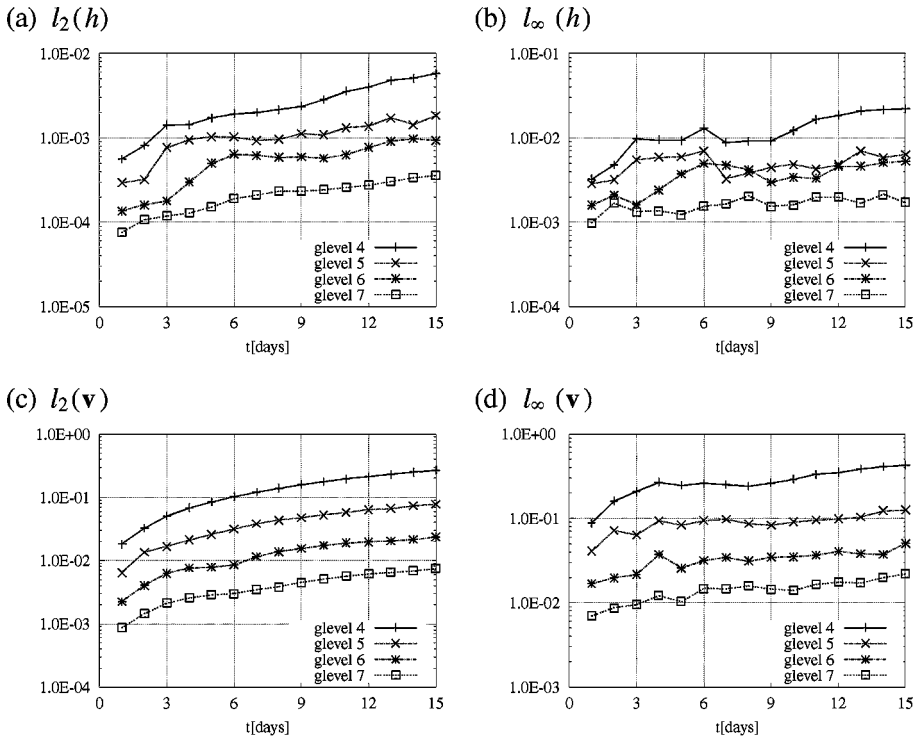

FIG. 15. The temporal variations of error norms for test case 5.

numerical solution is converging to the exact solution with first-order accuracy. Stuhne and Peltier [22] noted that the degradation is the result of the combined contribution of spatial and temporal truncation errors, computational noise, numerical imprecision, and other factors.

In order to investigate the convergence property of our model, we perform the simulations from glevel 4 up to 8 using the SPR-GC-grid. Values of the norms defined in Eq. (17) at $t =$ 5 days are plotted in Fig. 12, where the thick solid line indicates the quadratic convergence. We can see that all the norms become smaller along the ideal line as the resolution increases. These results would be reasonable, because the accuracies of all the operators are in the second order, as previously shown in Fig. 8.

5.3. Test Case 5: Zonal Flow over an Isolated Mountain

Test case 5 has a dynamic evolution of flow. The initial condition is similar to that in test case 2, that is, the velocity field is the solid body rotation and the height field is in the geostrophic balance. The reference depth and the maximum flow speed are set as $h_0 = 5960$ m and $u_0 = 20$ m/s, respectively. A mountain whose height is 2000 m is located at 30°N, 90°W. The detail formulation of the mountain is shown in Eq. (134) in Williamson *et al.* [19]. Total integration time is 15 days.

We perform this test case with our icosahedral model using the SPR-GC-grid without hyperviscosity. The time intervals are set to $\Delta t = 480,\ 240,\ 120$, and 60 s for glevel 4, 5, 6, and 7, respectively. Figure 13 shows the snapshot of h at 15 days with glevel 6. In this figure, contour lines are plotted on all of triangular elements using the raw data distributed

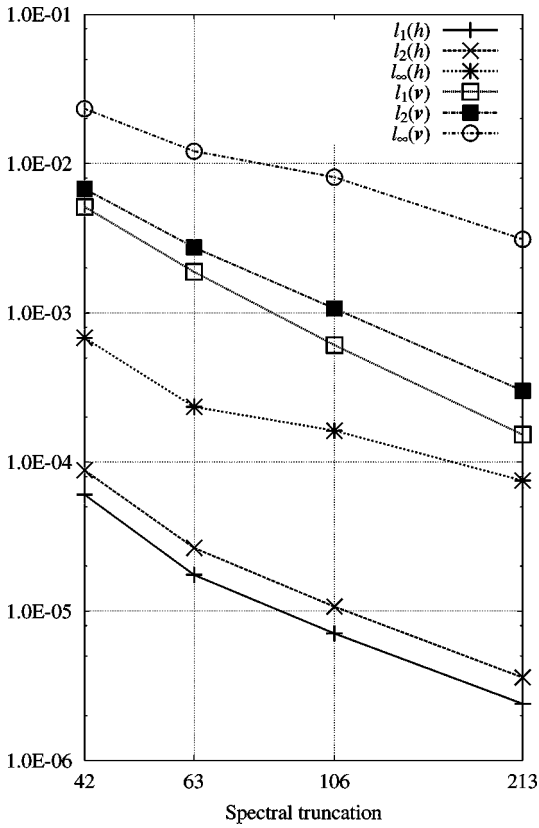

FIG. 16. Convergence properties of error norms of spectral results for test case 3 at 15 days. The T-426 spectral solution is employed as the reference solution.

on the icosahedral grid points. In spite of the absence of viscosity, the grid noise does not appear so that the contour lines are smoothly curved.

Since there is no analytic solution in this test case, a reference solution is obtained from integration of our spectral model[3] with T-213. For this spectral calculation, the vorticity-divergence form is used as the equation system. The vorticity, divergence, and geopotential are explicitly solved, and velocity is solved by Laplacian inversion of vorticity and divergence. The temporal evolution is performed using the fourth-order Runge–Kutta method and the time interval is set as 7364 time steps for a one-day simulation.

We process the spectral results as follows. Since we have the spectral coefficients by the simulations, we construct the data of spectral method on the icosahedral grid points by using the coefficients of spherical harmonics. Subtracting the icosahedral result from them, we can obtain the differences between the two data sets. Figure 14 shows the height field differences from the T-213 spectral model result at $t = 15$ days for glevel 4 up to 7. The large phase errors which appear in the lowest resolution become reduced with increasing resolution. There are some noise-like errors around the mountain for glevel 5 and 6. As described previously, this test case is performed without hyperviscosity, so that high wavenumber components generated by the nonlinear effect, which is large near the mountain, are not eliminated. The noise-like errors may be caused by the nonlinear effect.

[3] Several subroutines in ispack-0.5 [26] are used.

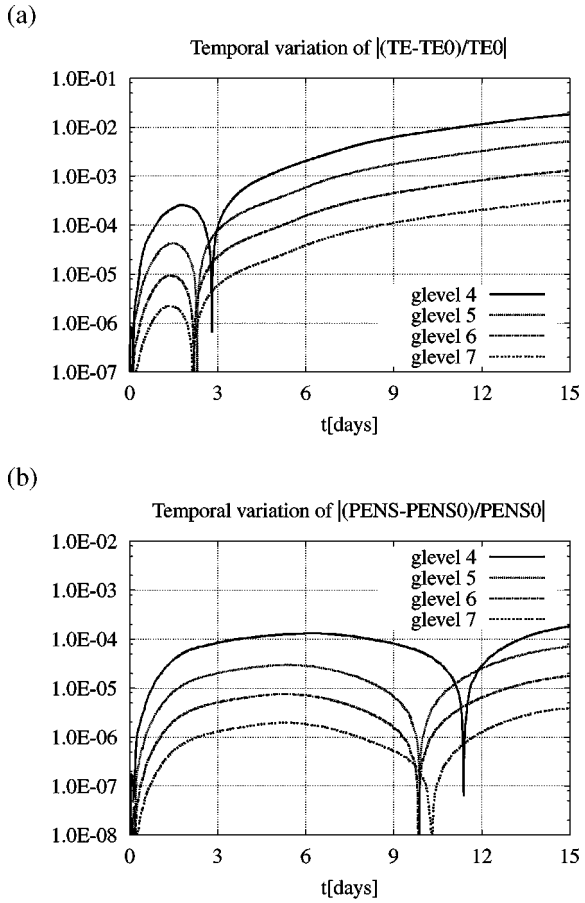

FIG. 17. Dissipation rates of total energy and potential enstrophy for test case 5.

The temporal evolutions of the l_2 and l_∞ norms of h and $\mathbf{v}$ are shown in Fig. 15. The globally averaged errors l_2 are reduced with increasing resolution as shown in Figs. 15a and 15c. The local errors l_∞ are also reduced as shown in Figs. 15b and 15d. Although there is a little degradation of accuracy for $l_\infty(h)$ from glevel 5 to 6, the value of $l_\infty(h)$ decreases again from glevel 6 to 7.

We have employed the T-213 spectral solution as the reference solution and assumed that it represents the "true" solution. However, it should be noted that the reference solution may not exactly be the "true" solution. To examine this issue, using our spectral model, we perform simulations for spectral truncation 42, 63, 106, 213, and 426. Figure 16 shows the error norms against the T-426 result at 15 days. Jakob-Chien *et al.* [27] also performed test case 5 simulations for T-42 and T-63 and showed the error norms against T-213. Our norms for T-42 and T-63 are somewhat smaller than their norms. The convergence speed of norms between T-42 and T-63 by our model is comparable to that of their model. As shown in Fig. 16, the convergence speed is not as high as expected from the spectral accuracy criterion, even in higher resolutions. Several reasons for this can be speculated. One of the main reasons would be that the shape of mountain is not differentiable, as pointed out by Jakob-Chien *et al.* [27]. Figure 16 suggests that the T-213 result, that is, our reference solution, includes at least errors of the order shown against the "true" solution. In comparison

TABLE II
The Hyper Viscosity Coefficients Used in Test Case 5

Viscosity coefficient: ν [m^4/s]	E-folding time: T_{ef} [h]
1.39681×10^{15}	0.5
6.98406×10^{14}	1
3.49203×10^{14}	2
1.74601×10^{14}	4
8.73007×10^{13}	8
4.36503×10^{13}	16
2.18251×10^{13}	32

with the icosahedral results of glevel 7 (Fig. 15), the norm errors of T-213 is one-tenth of those errors. So, we can say that the solution of T-213 can be treated as a reference solution until glevel 7. However, its validity may be reduced as compared to icosahedral results with much higher resolutions.

One of the purposes in test case 5 is to investigate the global conservation properties of models. Since our model is based on the finite volume representation, mass h^* is

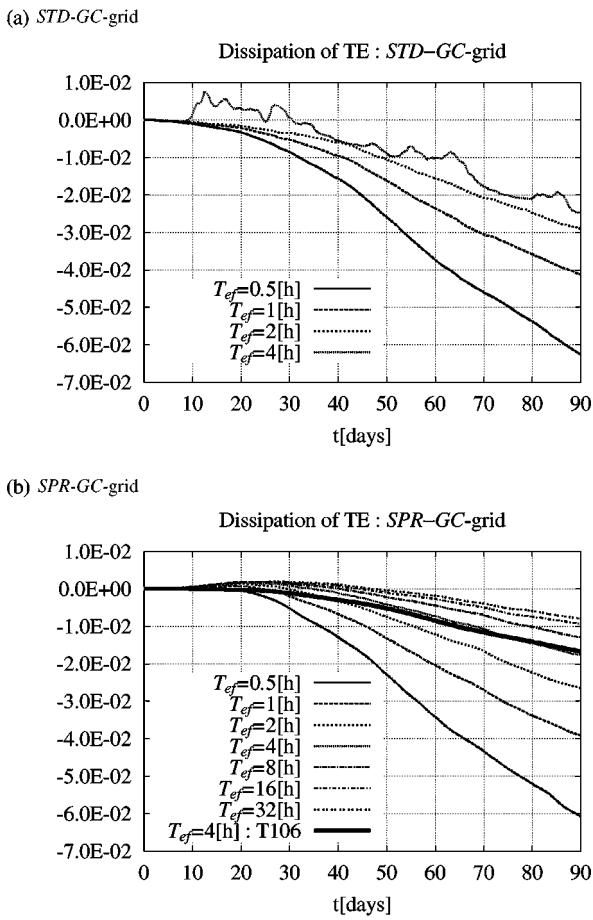

FIG. 18. Temporal variations of ΔTE for the 90 days simulations. (a) the STD-GC-grid and (b) the SPR-GC-grid.

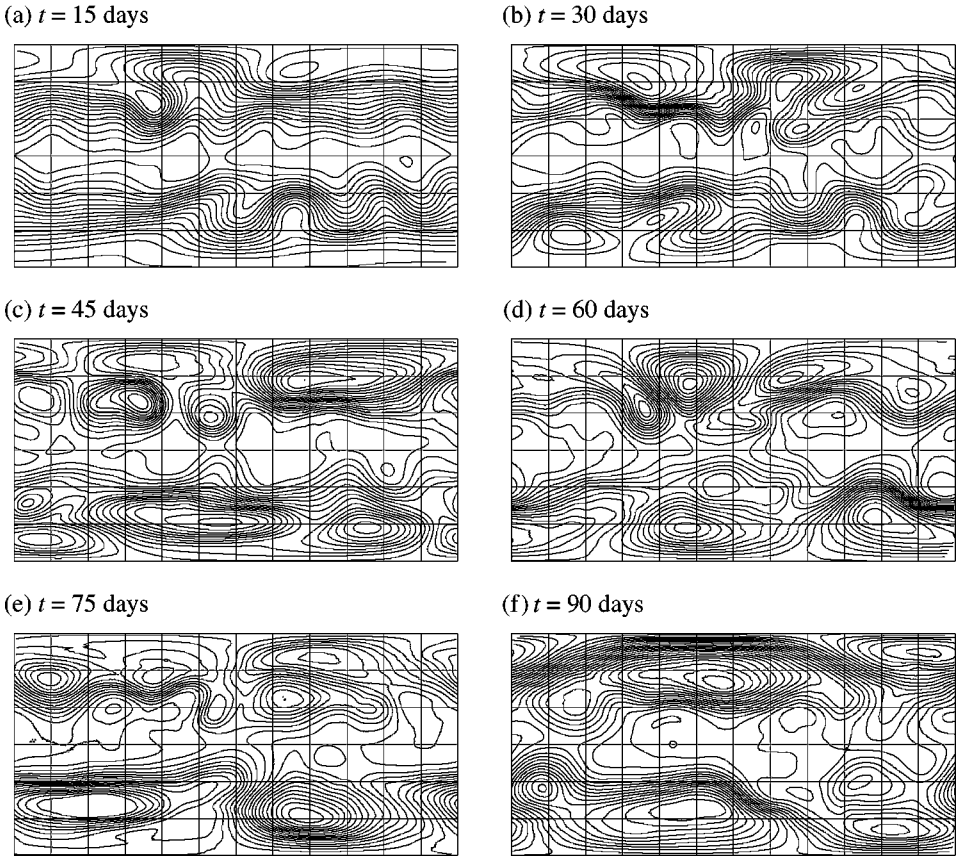

FIG. 19. Height field for the 90 days simulations with $T_{ef} = 32$ hours using the SPR-GC-grid.

perfectly conserved. In our model, the vorticity ζ and divergence $\delta(=\nabla \cdot \mathbf{v})$ are not prognostic variables. If we define these quantities diagnostically as Eqs. (9) and (10), they are also conserved.

We check the conservation of total energy *TE* and potential enstrophy *PE* defined as

$$TE = \frac{1}{4\pi a^2} \int\int \left(\frac{1}{2} h^* \mathbf{v} \cdot \mathbf{v} + \frac{1}{2} g\left(h^2 - h_s^2\right) - E_{p0} \right) d\sigma \tag{25}$$

$$PE = \frac{1}{4\pi a^2} \int\int \frac{1}{2h^*} (\zeta + f)^2 \, d\sigma, \tag{26}$$

where E_{p0} denotes the potential energy in the initial state and $d\sigma$ denotes the infinitesimal element of area. The definition of total energy in Eq. (25) is the same as that of Stuhne and Peltier [22] but different from that of Williamson *et al.* [19]. The difference rates from initial values for *TE* and *PE* are defined as

$$\Delta TE = \frac{TE - TE_0}{TE_0} \tag{27}$$

$$\Delta PE = \frac{PE - PE_0}{PE_0}, \tag{28}$$

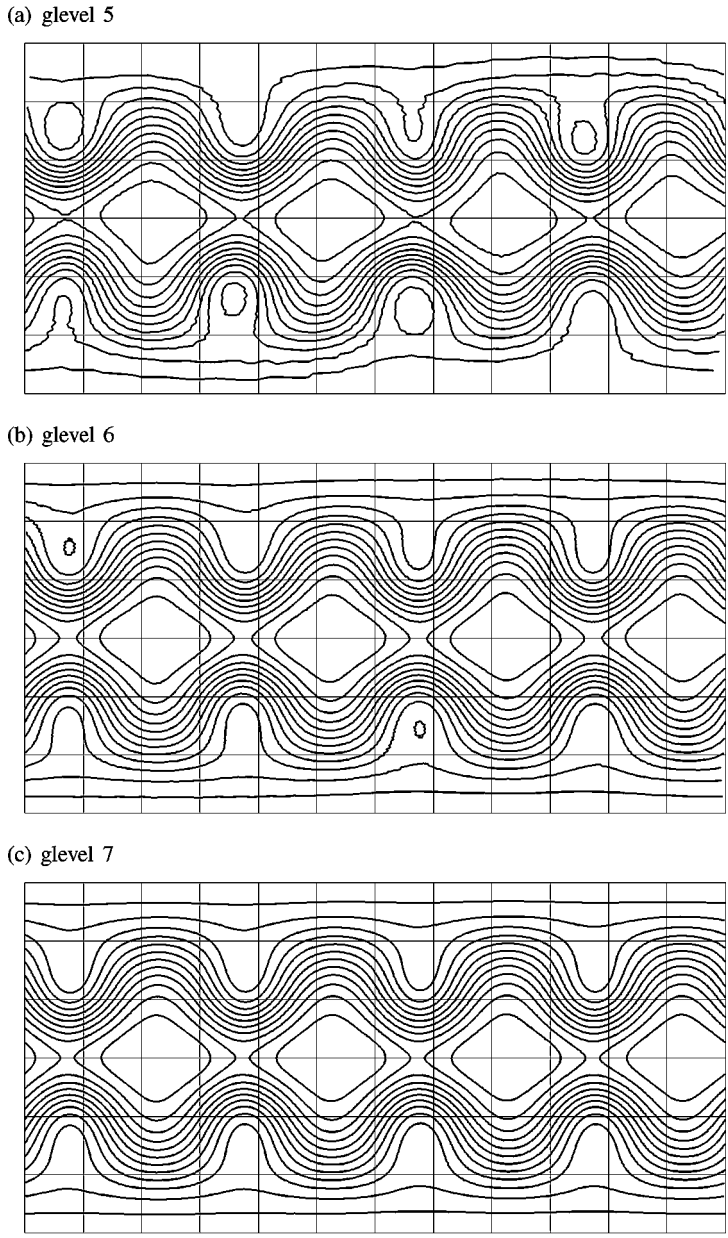

FIG. 20. Height field for test case 6 at the 14 days. Contour intervals are 200 m.

where TE_0 and PE_0 are the initial values. Figure 17 shows the temporal variations of $|\Delta TE|$ and $|\Delta PE|$. The rapid decreases near 2 days for $|\Delta TE|$ and near 10 days for $|\Delta PE|$ are due to the change of sign of ΔTE and ΔPE. The differences decrease in the quadratic sense as the increment of glevel. Thus, conservative quantities also have the second-order accuracy.

A remarkable performance using the SPR-GC-grid is demonstrated in the long-time simulation based on test case 5. The total simulation time is 90 days and the number of

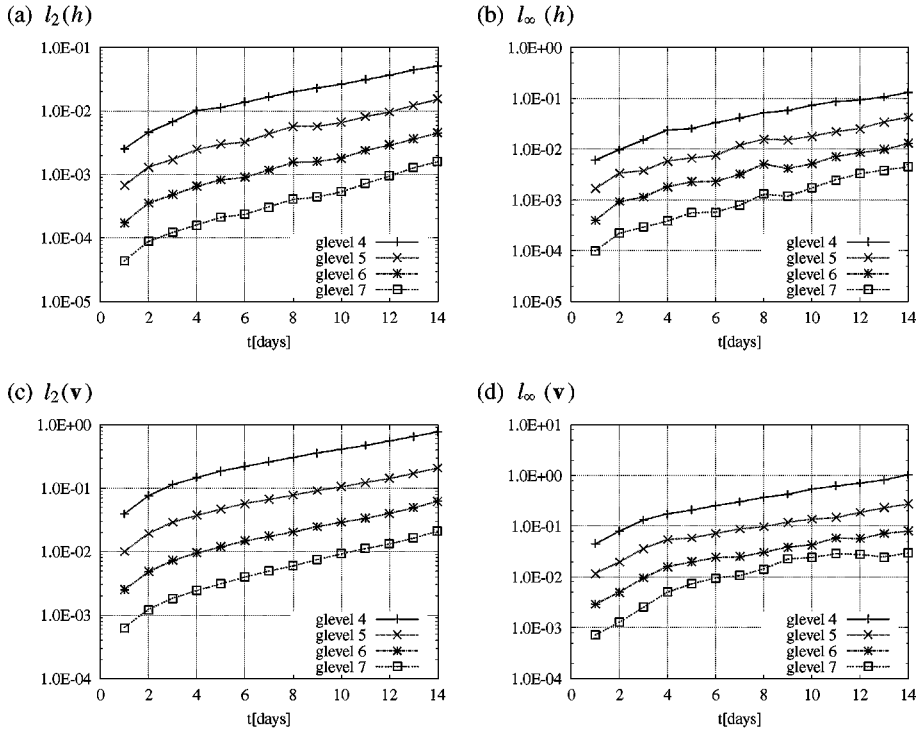

FIG. 21. The temporal variations of error norms for test case 6.

glevel is 6. Since the nonlinear term generates high wavenumber components in this case, the fourth-order hyperviscosity term defined as Eq. (12) is added to the momentum equation. The used coefficients are shown in Table II, where T_{ef} means the e-folding time for waves of two-grid-scale wavelength. Figure 18a shows the temporal variation for dissipation of *TE* defined as Eq. (27) using the STD-GC-grid. Total energies for $T_{ef} = 0.5$, 1, and 2 hours smoothly decay. However, the variation for $T_{ef} = 4$ hours includes a small fluctuation. It is suggested from investigation of height field that the small fluctuation of temporal history of ΔTE is caused by the amplifying nonphysical grid noise, which intermittently appears during simulation times. Figure 18b shows the same figure as Fig. 18a but using the SPR-GC-grid. For all of simulations using this grid system, total energies decay smoothly. The height fields for $T_{ef} = 32$ hours are shown in Fig. 19. In Fig. 18b, the spectral model result of T-106 for $T_{ef} = 4$ hours is also shown. The history of its decay after 50 days is in good agreement with that of the icosahedral result of the SPR-GC-grid for the same viscosity.

5.4. Test Case 6: Rossby–Haurwitz Wave

The Rossby–Haurwitz wave has been used for performance check of models since it was proposed by Phillips [10]. It is analytic solution of the nondivergent barotropic equation. Historically, this wave was used for nondivergent barotropic models based on the icosahedral grid at the first stage [9, 8]. Williamson *et al.* [19] introduced the Rossby–Haurwitz wave as one of the standard tests for shallow water models with a simple set of parameters.

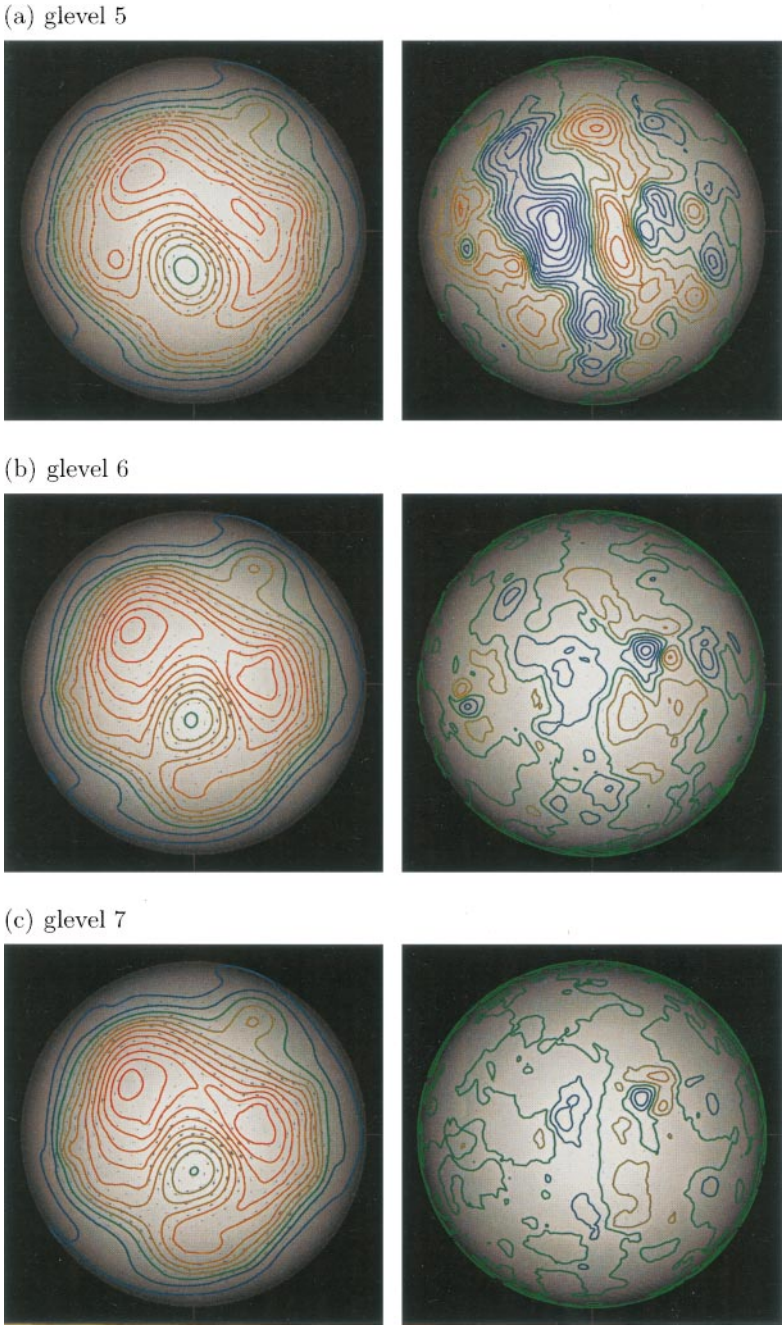

FIG. 22. Height field (left) and difference height field (right) from the T-213 spectral results for test case 7 at 5 days. The viewpoint of these figures are at the north pole. Contour intervals are 100 m for left figures and 30 m for right figures.

Since the shallow water equations include gravity waves, it is not guaranteed for the initial balance to remain during temporal evolution. The stability of zonal waves in the shallow water equations, which is well discussed in Hoskins [28] and Thuburn and Li [29], is not concerned here. In this paper, we deal with T-213 spectral results as the reference solutions

as in test case 5. The initial condition is the same as Eqs. (141)–(149) in Williamson *et al.* [19]. We perform simulations of this test case for glevel 5, 6, and 7 without viscosity. The time intervals are the same as those of test case 5.

Figure 20 shows the height fields using the SPR-GC-grid at 14 days. The equatorial symmetry is broken in the field of glevel 5 (Fig. 20a). This is obviously due to the asymmetry of the grid structure. Heikes and Randall [17] proposed the twisted icosahedral grid to avoid these errors. However, as resolution increases, the asymmetric errors become small (Fig. 20b and 20c). The l_2 and l_∞ norms against the reference solution are shown in Fig. 21. Convergence properties are better than those of test case 5 (Fig. 15). The reason for this would be that high wavenumber components are not large in test case 6.

5.5. Test Case 7: Analyzed 500 mb Height and Wind Field Initial Conditions

The final test case is to imitate real atmospheric motions. The initial condition is based on data at 0000 GMT 21 December 1978 [30]. We perform simulations in this case using the SPR-GC-grid from glevel 5 to 7. The hyperviscosity coefficients are set so that e-folding time of decay for the two-grid-scale wave corresponds to 4 hours, that is, $\nu = 2.7936 \times 10^{15}$, 1.7460×10^{14}, and 1.0913×10^{13} for glevel 5, 6, and 7, respectively. The time intervals are the same as those of test case 5 or 6.

Figure 22 shows the height and velocity fields at 5 days and the differences from the T-213 spectral model result. Our solutions for glevel 5 and 6 shown in Fig. 22a and 22b are in good agreement with those of Heikes and Randall [18] (see Figs. 19 and 20 in [18]). In glevel 7 (Fig. 22c), there is better correspondence to the T-213 spectral solution. Thus, the icosahedral model solution is well converged to the reference solution in the case of realistic flows as well.

6. CONCLUSIONS

We develop a new shallow water model on the modified icosahedral grid. The vector invariant form is employed as the momentum equation. The discretization of equations is based on the finite volume method. A modification of the grid is that the locations of grid points are moved to the gravitational centers of the control volumes. By this modification, the accuracy of differential operators is improved. In order to reduce the systematic grid noise, the grid system is also modified by solving the spring dynamics. By the combination of the above two modifications, we can obtain the ideal convergences for numerical operators as shown in Fig. 8 and the grid noise is well reduced as demonstrated by the long time-simulation for the zonal geostrophic problem (test case 2 of [19]). Using the modified grid, the excellent performances are also obtained for the other test cases. Apparently, the modification of grid by spring dynamics and gravitational-centered relocation is a fine step both for numerical accuracy and for numerical stability.

Our goal is the development of the high resolution climate model which couples the atmospheric and oceanic general circulation models to help us understand the mechanism of global changes such as the global warming. Especially, we intend that the resolution eventually increases up to cloud resolving scale (10 km or less) for the atmospheric model. The development of the shallow water model in this study is the first step to the goal. We showed that if the icosahedral grid is employed as the horizontal grid system, there would be no problem on the numerical accuracy of operators in the high resolution calculation.

From the viewpoint of computational efficiency, we are now further developing this model for implementations in massively parallel computers and investigating the computational efficiency in comparison with the spectral method.

APPENDIX A

In this section, we describe how to obtain Eq. (4) from Eq. (3). An arbitrary tangential plane on the sphere is considered. We put an x-y-z Cartesian coordinate in which x-y planes are parallel to the tangential plane and the origin corresponds to the contact point between the spherical surface and the plane. z is directed to the vertical.

At the origin, the relations are satisfied,

$$w = 0, \quad \frac{\partial u}{\partial z} = \frac{\partial v}{\partial z} = 0, \tag{A.1}$$

where, u, v, and w are x-, y-, and z-components of velocity vector $\mathbf{v}$. Using Eq. (A.1), the vorticity vector $\boldsymbol{\omega}$ at the origin can be written as

$$\boldsymbol{\omega} = \nabla \times \mathbf{v} = \left(\frac{\partial w}{\partial y}, -\frac{\partial w}{\partial x}, \frac{\partial v}{\partial x} - \frac{\partial u}{\partial y} \right). \tag{A.2}$$

The x- and y-components of $\boldsymbol{\omega}$ do not vanish because of curvature of the spherical surface. From the constraint that the normal component of velocity vector to the spherical surface equals to zero, we can obtain the horizontal derivatives of w at the origin as

$$\frac{\partial w}{\partial y} = -\frac{v}{a}, \quad \frac{\partial w}{\partial x} = -\frac{u}{a}. \tag{A.3}$$

We can interpret Eqs. (A.2) and (A.3) to the following formulation:

$$\boldsymbol{\omega} = \zeta \hat{\mathbf{k}} + \hat{\mathbf{k}} \times \frac{\mathbf{v}}{a}. \tag{A.4}$$

This vector formulation is true at any point on the spherical surface. From Eq. (A.4), we can obtain the following equation:

$$\boldsymbol{\omega} \times \mathbf{v} = \zeta \hat{\mathbf{k}} \times \mathbf{v} - \frac{\mathbf{v} \cdot \mathbf{v}}{a} \hat{\mathbf{k}}. \tag{A.5}$$

Equation (4) is derived from Eq. (3) with Eq. (A.5).

APPENDIX B

In Section 4, we see the increase of computational accuracy by the move of the location of grid point to the gravitational center of control volume. In this section, the mathematical proof of this fact is given. First, consider an arbitrary triangle on a flat plane and let the positions of vertices be (x_1, y_1), (x_2, y_2), and (x_3, y_3) in counterclockwise order (Fig. 23a). We define the quadratic function $u(x, y)$ as

$$u(x, y) = Ax^2 + By^2 + Cxy + Dx + Ey + F, \tag{B.1}$$

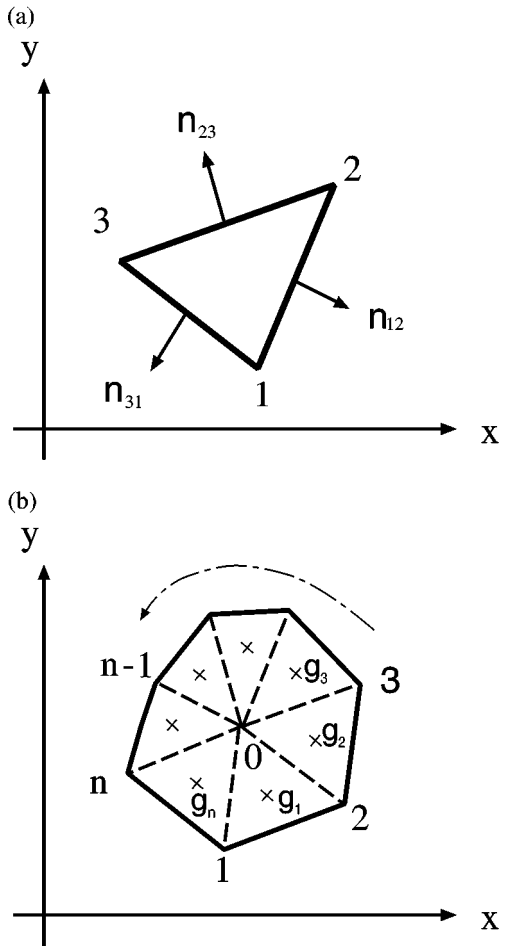

FIG. 23. (a) Schematic figure of a triangle on a flat plane. (b) That of a polygon.

where A, B, C, D, E, and F are constant. The exact solution of gradient of u is obtained from Eq. (B.1) as

$$[\nabla u]_t(x, y) = \begin{pmatrix} D + 2Ax + Cy \\ E + Cx + 2By \end{pmatrix}. \tag{B.2}$$

Integrating u along three sides of triangles, we can obtain an estimation value of ∇u on this triangle as

$$[\nabla u]_c = \frac{1}{A} \oint u\mathbf{n}\, dl = \frac{1}{A} \left[\int_1^2 u\mathbf{n_{12}}\, dl_{12} + \int_2^3 u\mathbf{n_{23}}\, dl_{23} + \int_3^1 u\mathbf{n_{31}}\, dl_{31} \right], \tag{B.3}$$

where $\mathbf{n}$ and dl denote the normal vector to the side and the infinitesimal line element. Subscript ij ($i \neq j$) means value along side ij from the point i to the point j. A is the area of the triangle. The equation of line ij is written as

$$y - y_i = \frac{y_j - y_i}{x_j - x_i}(x - x_i). \tag{B.4}$$

The terms $\mathbf{n}_{ij}$, d_{ij}, and A can be expressed as

$$\mathbf{n}_{ij} = \frac{1}{\sqrt{(x_j - x_i)^2 + (y_j - y_i)^2}} \begin{pmatrix} y_j - y_i \\ -(x_j - x_i) \end{pmatrix}, \tag{B.5}$$

$$dl_{ij} = \frac{\sqrt{(x_j - x_i)^2 + (y_j - y_i)^2}}{x_j - x_i}\, dx, \tag{B.6}$$

$$A = \frac{1}{2}(x_1 y_2 + x_2 y_3 + x_3 y_1 - x_3 y_2 - x_2 y_1 - x_1 y_3) \tag{B.7}$$

Substituting Eqs. (B.4)–(B.7) to Eq. (B.3), we can obtain

$$[\nabla u]_c = \begin{pmatrix} D + 2A(x_1 + x_2 + x_3)/3 + C(y_1 + y_2 + y_3)/3 \\ E + C(x_1 + x_2 + x_3)/3 + 2B(y_1 + y_2 + y_3)/3 \end{pmatrix}. \tag{B.8}$$

From Eqs. (B.2) and (B.8), we can say that the estimation value $[\nabla u]_c$ corresponds to the exact solution $[\nabla u]_t$ at the gravitational center of triangle.

We can prove that this is true for an arbitrary polygon as follows. Again, the quadratic function $u(x, y)$ is defined as Eq. (B.1). As shown in Fig. 23b, an n-th polygon is divided into n triangles. The gravitational center and area of the triangle $0 - k - k + 1$ are denoted by $\mathbf{g}_k = (g_{kx}, g_{ky})$ and A_k, respectively. In a similar way to Eq. (B.3), the gradient of u on the polygon is estimated as

$$\begin{aligned}
[\nabla u]_c &= \frac{1}{A}\left[\int_1^2 u\mathbf{n}_{12}\, dl_{12} + \int_2^3 u\mathbf{n}_{23}\, dl_{23} + \cdots + \int_n^1 u\mathbf{n}_{n1}\, dl_{n1}\right] \\
&= \frac{1}{A}\left[\left(\int_0^1 u\mathbf{n}_{01}\, dl_{01} + \int_1^2 u\mathbf{n}_{12}\, dl_{12} + \int_2^0 u\mathbf{n}_{20}\, dl_{20}\right)\right. \\
&\quad + \left(\int_0^2 u\mathbf{n}_{02}\, dl_{02} + \int_2^3 u\mathbf{n}_{23}\, dl_{23} + \int_3^0 u\mathbf{n}_{30}\, dl_{30}\right) + \cdots\cdots \\
&\quad \left. + \left(\int_0^n u\mathbf{n}_{0n}\, dl_{0n} + \int_n^1 u\mathbf{n}_{n1}\, dl_{n1} + \int_1^0 u\mathbf{n}_{10}\, dl_{10}\right)\right] \\
&= \frac{1}{2}\left[\oint_{012} u\mathbf{n}\, dl + \oint_{023} u\mathbf{n}\, dl + \cdots + \oint_{0n1} u\mathbf{n}\, dl\right],
\end{aligned} \tag{B.9}$$

where $\oint_{0ij}$ denotes the line integral around the triangle $0ij$. Note that the second line in Eq. (B.9) is derived from the first line with the relation of $\mathbf{n}_{ij} = -\mathbf{n}_{ji}$. From the conclusion in the previous paragraph, we can write the line integral around the triangle $0 - k - k + 1$ as

$$\oint_{0kk+1} u\mathbf{n}\, dl = A_k[\nabla u]_t(\mathbf{g}_k). \tag{B.10}$$

Substituting Eq. (B.10) into Eq. (B.9), we can obtain the following formulation for the estimation value:

$$[\nabla u]_c = \sum_{i=1}^{n} A_i[\nabla u]_t(\mathbf{g}_i) \Bigg/ \sum_{i=1}^{n} A_i. \tag{B.11}$$

Using Eq. (B.2), Eq. (B.11) can be written as

$$[\nabla u]_c = \begin{pmatrix} D + 2AG_x + CG_y \\ E + CG_x + 2BG_y \end{pmatrix} = [\nabla u]_t(\mathbf{G}), \tag{B.12}$$

where $\mathbf{G} \equiv (G_x,\ G_y) = (\sum_{i=1}^n A_i g_{ix}/\sum_{i=1}^n A_i,\ \sum_{i=1}^n A_i g_{iy}/\sum_{i=1}^n A_i)$. The vector $\mathbf{G}$ represents the gravitational center of the n-th polygon. Thus, we can say that for an arbitrary polygon, the estimation value $[\nabla u]_c$ corresponds to the exact solution $[\nabla u]_t$ at its gravitational center.

Now, let the function u be a general function and the origin of coordinates be near the central point of the n-th polygon. Note that the origin does not need to correspond to the gravitational center. We can expand u to the Taylor series around the origin as

$$\begin{aligned} &u(x,\ y) = \hat{u}(x,\ y) + \varepsilon, \\ &\hat{u}(x,\ y) \equiv u|_O + \left.\frac{\partial u}{\partial x}\right|_O x + \left.\frac{\partial u}{\partial y}\right|_O y + 2\left.\frac{\partial^2 u}{\partial y \partial y}\right|_O xy + \left.\frac{\partial^2 u}{\partial x^2}\right|_O x^2 + \left.\frac{\partial^2 u}{\partial y^2}\right|_O y^2, \end{aligned} \tag{B.13}$$

where ε represents the residual of which the leading terms are cubic polynomials.

Differentiating Eq. (B.13), we can obtain

$$[\nabla u]_t(\mathbf{r}) = [\nabla \hat{u}]_t(\mathbf{r}) + [\nabla \varepsilon]_t(\mathbf{r}). \tag{B.14}$$

This equation can be rewritten as

$$[\nabla u]_t(\mathbf{r}) = [\nabla \hat{u}]_t(\mathbf{G}) + J(\mathbf{r} - \mathbf{G}) + [\nabla \varepsilon]_t(\mathbf{r}), \tag{B.15}$$

where J is the following matrix:

$$J = 2\begin{pmatrix} \left.\frac{\partial^2 u}{\partial x^2}\right|_O & \left.\frac{\partial^2 u}{\partial x \partial y}\right|_O \\ \left.\frac{\partial^2 u}{\partial x \partial y}\right|_O & \left.\frac{\partial^2 u}{\partial y^2}\right|_O \end{pmatrix}. \tag{B.16}$$

On the other hand, by the same way as Eq. (B.9), the estimation value has the following form:

$$[\nabla u]_c = [\nabla \hat{u}]_c + [\nabla \varepsilon]_c. \tag{B.17}$$

Because the function $\hat{u}(x,\ y)$ is a quadratic function, the relation of $[\nabla \hat{u}]_c = [\nabla \hat{u}]_t(\mathbf{G})$ is satisfied. This leads to the error owing to the estimation:

$$[\nabla u]_c - [\nabla u]_t(\mathbf{r}) = [\nabla \varepsilon]_c - [\nabla \varepsilon]_t(\mathbf{r}) - J(\mathbf{r} - \mathbf{G}). \tag{B.18}$$

Since the leading terms of ε is cubic polynomials, the first term on the right-hand side has the magnitude of order of Δd^2, where Δd denotes the reference length, such as $\sqrt{A}$. The second term also has the magnitude of order of Δd^2, because components of $[\nabla \varepsilon]_t(\mathbf{r})$ itself contain quadratic polynomials. The third term, however, does not vanish in the second-order sense, because $|\mathbf{r} - \mathbf{G}| \sim \mathcal{O}(\Delta d)$. It is obvious that this term should be zero only if $\mathbf{r} = \mathbf{G}$. Thus, we can conclude that for the gradient operator the relocation of the grid point to the gravitational center of control volume provides the increase of accuracy. Also, as for the divergence operator and the curl operator, we can show by the similar way that the same is true.

TABLE III
Comparison of the Ratios of the Maximum Grid Interval to the Minimum Grid Interval among the Grid Systems in This Study

glevel	STD-grid	STD-GC-grid	SPR-GC-grid	SPR-NL-GC-grid
3	1.311	1.311	1.508	1.235
4	1.331	1.331	1.663	1.256
5	1.336	1.336	1.824	1.272
6	1.337	1.337	1.990	1.285
7	1.337	1.337	2.156	1.295

APPENDIX C

In the text, we show the advantage of using the SPR-GC-grid both for the numerical accuracy and for the numerical stability. However, the grid modification causes a trivial problem concerning the homogeneity of grid. Table III shows the ratios of maximum grid interval to minimum grid interval for the STD-grid, the STD-GC-grid, and the SPR-GC-grid. The local grid interval is estimated by the square root of the area of control volume. The values of the STD-grid and the STD-GC-grid are the same because of the same control volumes. They are converging to the value of 1.337 as the increment of glevel, so the homogeneity of the grid can be maintained. On the other hand, the value of the SPR-GC-grid gradually increases as the increment of glevel, though its increase is small. We can remedy this defect by replacing the linear spring formula in Eq. (20) by an appropriate nonlinear spring formula. For example, instead of $\bar{d}$ in Eq. (20), we can formulate the length of spring as

$$\bar{d}_i = \frac{1}{2}\bar{d}\left(\frac{\bar{A}}{A_0} + \frac{\bar{A}}{A_i}\right), \tag{C.1}$$

where $\bar{A}$ denotes the global average of area of control volume and A_i denotes the area at point P_i. Such an inclusion of feedback of area in dynamics makes the grid homogeneous. We call this grid system the SPR-NL-GC-grid. The ratios of maximum grid interval to minimum grid interval at $\beta = 0.8$, are shown in Table III, where the SPR-NL-GC-grid is more homogeneous than the STD-grid and the STD-GC-grid. Of course, since the geometrical quantities are relatively monotonic also in the SPR-NL-GC-grid, the noise-reduction can be expected.

ACKNOWLEDGMENTS

The authors are very grateful to Dr. Detlev Majewski in Deutscher Wetterdienst (DWD) and to Dr. David R. Randall of Colorado State University for useful discussions on private communication. We also thank our colleagues related with this work, especially Dr. Yoshio Kurihara and Dr. Taroh Matsuno, who have always encouraged us to pursue model development.

REFERENCES

1. R. Suda, High performance computation of spherical harmonic transform, in *IPSJ SIG Notes*, Vol. 98-HPC-71, p. 7 (Tsukuba, May 1998).

2. R. Suda, A fast spherical harmonics transform algorithm, in *IPSJ SIG Notes*, Vol. 98-HPC-73 (Sendai, Oct. 1998), p. 37.
3. P. J. Roache, *Computational Fluid Dynamics* (Hermora, 1976).
4. K. Bryan, S. Manabe, and R. C. Pacanowski, A global ocean-atmosphere climate model part II. The oceanic circulation, *J. Phys. Oceanogr.* **5**, 30 (1975).
5. L. L. Takacs and R. Balgovind, High latitude filtering in global grid point models, *Mon. Weather Rev.* **111**, 2005 (1983).
6. A. Staniforth and J. Côté, Semi-Lagrangian integration schemes for atmospheric models, *Mon. Weather Rev.* **119**, 2206 (1991).
7. A. Priestley, A quasi-conservative version of the semi-Lagrangian advection scheme, *Mon. Weather Rev.* **121**, 621 (1993).
8. R. Sadourny, A. Arakawa, and Y. Mintz, Integration of the nondivergent barotropic vorticity equation with an icosahedral hexagonal grid for the sphere, *Mon. Weather Rev.* **96**, 351 (1968).
9. D. L. Williamson, Integration of the barotropic vorticity equation on a spherical geodesic grid, *Tellus* **20**, 642 (1968).
10. N. A. Phillips, Numerical integration of the primitive equation on the hemisphere, *Mon. Weather Rev.* **87**, 333 (1959).
11. R. Sadourny, Numerical integration of the primitive equations on a spherical grid with hexagonal cells, in *Proceedings of the WMO/IUGG Symposium on Numerical Weather Prediction in Tokyo, Tech. Rep. of JMA* (Japan Meteorological Agency, Nov. 26–Dec. 4, 1969), pp. VII45–VII52.
12. D. L. Williamson, Integration of the primitive barotropic model over a spherical geodesic grid, *Mon. Weather Rev.* **98**, 512 (1969).
13. Y. Masuda and H. Ohnishi, An integration scheme of the primitive equation model with an icosahedral-hexagonal grid system and its application to the shallow water equations, in *Short- and Medium-Range Numerical Weather Prediction. Collection of Papers Presented at the WMO/IUGG NWP Symposium, Tokyo, Aug. 4–8 1986* (Japan Meteorological Society, 1986), p. 317.
14. M. J. P. Cullen, Integration of the primitive equations on a sphere using the finite element method, *Q. J. R. Meteorol. Soc.* **100**, 555 (1974).
15. M. J. P. Cullen and C. D. Hall, Forecasting and general circulation results from finite element models, *Q. J. R. Meteorol. Soc.* **105**, 571 (1979).
16. J. W. Cooley and J. W. Turkey, An algorithm for the machine computation of complex fourier series, *Math. Comput.* **19**, 297 (1965).
17. R. H. Heikes and D. A. Randall, Numerical integration of the shallow-water equations on a twisted icosahedral grid. Part I: Basic design and results of tests, *Mon. Weather Rev.* **123**, 1862 (1995).
18. R. H. Heikes and D. A. Randall, Numerical integration of the shallow-water equations on a twisted icosahedral grid. Part II: A detailed description of the grid and analysis of numerical accuracy, *Mon. Weather Rev.* **123**, 1881 (1995).
19. D. L. Williamson, J. B. Drake, J. J. Hack, R. Jacob, and P. N. Swarztrauber, A standard test set for numerical approximations to the shallow water equations in spherical geometry, *J. Comput. Phys.* **102**, 211 (1992).
20. T. D. Ringler, R. H. Heikes, and D. A. Randall, Modeling the atmospheric general circulation using a spherical geodesic grid: A new class of dynamical cores, *Mon. Weather Rev.* **128**, 2471 (2000).
21. G. R. Stuhne and W. R. Peltier, Vortex erosion and amalgamation in a new model of large scale flow on the shere, *J. Comput. Phys.* **128**, 58 (1996).
22. G. R. Stuhne and W. R. Peltier, New icosahedral grid-point discretizations of the shallow water equations on the sphere, *J. Comput. Phys.* **148**, 23 (1999).
23. J. Thuburn, A PV-based shallow-water model on a hexagonal-icosahedral grid, *Mon. Weather Rev.* **125**, 2328 (1997).
24. J. Côté, A lagrange multiplier approach for the metric terms of semi-lagrangian models on the sphere, *Q. J. R. Meteorol. Soc.* **114**, 1347 (1988).
25. G. L. Browning, J. J. Hack, and P. N. Swarztrauber, A comparison of three numerical methods for solving differential equations on the sphere, *Mon. Weather Rev.* **117**, 1058 (1995).

26. K. Ishioka, ispack-0.5 (GFD Dennou Club), available at http://www.gfd-dennou.org/arch/ispack/, 2000.
27. R. Jakob-Chien, J. J. Hack, and D. L. Williamson, Spectral transform solutions to the shallow water test set, *J. Comput. Phys.* **119**, 164 (1995).
28. B. J. Hoskins, Stability of the Rossby–Haurwitz wave, *Q. J. R. Meteorol. Soc.* **99**, 723 (1973).
29. J. Thuburn and Y. Li, Numerical simulation of Rossby–Hauwitz waves, *Tellus* **52A**, 181 (2000).
30. H. Ritchie, Application of the semi-Lagrangian method to a spectral model of the shallow-water equations, *Mon. Weather Rev.* **116**, 1587 (1988).